

Multiparticle cumulant mapping for Coulomb explosion imaging: Calculations and algorithm

Chuan Cheng^{1,2,*}, Leszek J. Frasinski³, Gönenç Moğol¹, Felix Allum^{2,4}, Andrew J. Howard^{1,2,5}, Philip H. Bucksbaum^{2,4}, Ruaridh Forbes^{2,4}, and Thomas Weinacht^{1,†}

¹*Department of Physics and Astronomy, Stony Brook University, Stony Brook, New York 11794, USA*

²*Stanford PULSE Institute, SLAC National Accelerator Laboratory, Menlo Park, California 94025, USA*

³*Department of Physics, Imperial College London, Prince Consort Road, London SW7 2AZ, United Kingdom*

⁴*Linac Coherent Light Source, SLAC National Accelerator Laboratory, Menlo Park, California 94025, USA*

⁵*Department of Applied Physics, Stanford University, Stanford, California 94305, USA*



(Received 4 September 2023; accepted 7 February 2024; published 1 April 2024)

We present a versatile cumulant mapping algorithm for analyzing correlated particle emission, offering insights into complex electronic and nuclear dynamics. Recently, we have demonstrated the use of cumulant mapping to extract information-rich correlations between the momenta of multiple fragments produced in Coulomb explosion imaging experiments [C. Cheng *et al.*, *Phys. Rev. Lett.* **130**, 093001 (2023)]. We define cumulant mapping in terms of histograms, enabling fast computation of linear (additive) observables. However, applying the same algorithm to nonlinear (nonadditive) observables poses challenges, as the computation time of conventional estimators scales nonlinearly with data size. To overcome this, we develop estimators and an accompanying algorithm to enable computationally efficient estimation of the cumulant of interest. Comparisons of computation times and signal-to-noise ratios reveal the superior performance of our approach. This method is demonstrated on the (D^+ , D^+ , C^+ , O^+) dissociation channel of CD_2O^{4+} produced in a strong-field ionization experiment. Additionally, Poisson statistics are used to simulate the two methods and provide insights into the efficiency of our algorithm. The proposed methodology unlocks efficient computation of cumulant mapping for a broader range of complex systems and observables, such as the laser pulse dependence of ionization dynamics.

DOI: [10.1103/PhysRevA.109.042802](https://doi.org/10.1103/PhysRevA.109.042802)

I. INTRODUCTION

Measuring multiparticle correlation is at the core of many studies of the structure and dynamics of small molecules [1–13]. In particular, Coulomb explosion imaging (CEI) is of great interest because it can provide time-resolved information on molecular structure in the recoil frame. Through CEI, the structure of molecules can be inferred by analyzing the relative momenta of fragment ions coming from the parent molecular polycation. This technique allows investigation into many structural changes occurring in photoexcited molecules including isomerization [14–18], dissociation [11,12,19–27], roaming [28–31], and hydrogen migration [32,33]. Recently, both strong-field ionization and x-ray multiphoton ionization-induced CEI have yielded promising results in studies that make use of multiparticle correlations [12,15,24,28,34–38].

Covariance mapping has emerged as a valuable tool for investigating correlations among multiple variables in various research domains, including analytical chemistry, mass spectrometry, two-dimensional (2D) spectroscopy, and molecular imaging [39–42]. Recently, this methodology has been successfully applied to multiparticle correlation, encompassing twofold covariance, denoted as χ_2 , on molecules of biological

relevance [43–45], and molecular dimers and trimers embedded in helium nanodroplets [46–49]. Threefold covariance χ_3 has been used to study three-body CEI of molecular dissociation dynamics [7,50,51].

Starting from the fourth order, the n th-order covariance χ_n has contributions from pairwise correlations that are independent or separate from the full n -body correlations of interest. Consequently, nonzero correlation values can be observed even in the absence of collective correlations among all n fragments [52–54]. Cumulant mapping, represented by \varkappa_n , can be used to obtain the correct four-body or higher-body correlations [52,54].

An important aspect of analyzing covariance or cumulant measurements is the generation of histograms of meaningful observables based on these many-body correlations. The true many-body correlations, like momentum conservation of fragments, will stand out from statistical fluctuations when projected onto histograms of the appropriate observable. Earlier work has validated the efficacy of covariance in comparison with coincidence analysis [7,55,56], and the effectiveness of using covariance to isolate the signal of interest [41,54,57]. However, performing covariance analysis is often less intuitive than initially expected. There exists a gap between the symbols within the mathematical definition and their application in data analysis. Furthermore, there are a lack of suitable algorithms for calculating observable histograms, coupled with a limited discussion on the statistical

*chengcc1@stanford.edu

†thomas.weinacht@stonybrook.edu

or systematic errors associated with these measurements. In this study, we describe a practical algorithm that serves as a bridge, and hope to stimulate interest in further refinement of the algorithm.

In this paper, we show how to extend the cumulant formula, which produces a single number, to generalized cumulant mapping through histograms and convolution. As an example, we describe the algorithm for computing momentum-summed fourfold cumulant mapping of particles, as demonstrated on CEI of deuterated formaldehyde in earlier work [52].

However, when applying the same calculation to generate cumulant mapping for more complex observables, like the angle between fragments' momenta, or fragment momenta within a molecular frame, we find that it becomes excessively time consuming because the computational time or time complexity T follows a power law:

$$T(\widehat{\varkappa}_n) \sim S^n. \quad (1)$$

Here the circumflex denotes an estimator, \varkappa_n is the n th cumulant, S is the number of laser shots, which is a measure of the size of the data set, and n is the characteristic index of the power law, which is the same as the number of fragments involved in the cumulant mapping analysis. To compute cumulant mapping for these complicated observables that reflect many-body correlations, the calculations of certain terms involve products of expectation values, which leads to $n > 1$ and becomes more and more time consuming as the number of fragments involved increases.

While the computational timescales as shown in Eq. (1), the uncertainty or variance in the cumulant only converges as

$$\text{var}(\widehat{\varkappa}_n) \sim S^{-1}. \quad (2)$$

Here $\text{var}(\widehat{\varkappa}_n)$ is the variance of the cumulant estimator and shows its dependence on the number of laser shots S . To overcome the problem of increased computational complexity, we developed an algorithm based on an estimator that balances the computational and statistical efficiencies. This estimator can be computed in a much faster timescale $T(\widehat{\varkappa}_n) \sim S$, while also converging as $\text{var}(\widehat{\varkappa}_n) \sim S^{-1}$.

II. EXPERIMENTAL SETUP

Our experiments make use of a velocity map imaging (VMI) apparatus [58] outfitted with a TPX3CAM camera [59]. The laser pulses originate from a commercial amplified Ti:sapphire laser system, which produces 30-fs laser pulses with 1 mJ of energy at a repetition rate of 1 kHz. The pulses are focused into our VMI apparatus to ionize molecules.

The sample, deuterated formaldehyde, is obtained by sublimation of paraformaldehyde-D₂ (purity 98%, Sigma-Aldrich) at 50 °C–60 °C. The deuterated formaldehyde vapor then enters the sample chamber through a nozzle. By passing through a 200-μm diameter skimmer between the sample chamber and the VMI chamber, the skimmed molecular beam of sample molecules intersects the laser in the VMI apparatus.

The ionized fragments are accelerated toward the microchannel plates (MCP) and phosphor screen under velocity-mapping conditions. The fluorescence from hits on the phosphor screen is imaged onto the camera with an $f/0.95$ lens. The 1-ns precision of the TPX3CAM can resolve the ion momenta along the time-of-flight (ToF) direction, which can be used to reconstruct the full three-dimensional (3D) vector momenta of ions [7,34,59]. For the data presented here, the typical acquisition time was approximately 20 min, with on average 8 ions detected per shot (roughly 1.4 H⁺, 1.7 D⁺, 0.68 C⁺, 0.68 O⁺, 0.2 CO⁺ and a few other ion species per shot). The detection efficiency of our apparatus is estimated to be between $\eta = 60\%$ and 90% per particle [60] and the resulting fourfold channel would have an overall detection efficiency of around $\eta^4 = 13\%$ to 65% [54].

III. CALCULATION OF CUMULANT MAPPING FOR ADDITIVE OBSERVABLES

In order to compute the fourth-order cumulant map, we start by expanding the definition of the fourth cumulant into a form that has products of expectation values, rather than nested expectation values. This adaptation allows us to compute more complicated observables, such as momentum sums and the fragment recoil frame, as shown in earlier work [52]. The expansion is straightforward, following the definition of the n th-order covariance χ_n and cumulant \varkappa_n [54]:

$$\begin{aligned} \varkappa_4 &= \chi_4^{ABCD} - \sum^3 \chi_2^{AB} \chi_2^{CD} \\ &= \langle (N^A - \langle N^A \rangle)(N^B - \langle N^B \rangle)(N^C - \langle N^C \rangle)(N^D - \langle N^D \rangle) \rangle - \sum^3 \langle (N^A - \langle N^A \rangle)(N^B - \langle N^B \rangle) \rangle \langle (N^C - \langle N^C \rangle)(N^D - \langle N^D \rangle) \rangle \\ &= \langle N^A N^B N^C N^D \rangle - \sum^4 \langle N^A \rangle \langle N^B \rangle \langle N^C \rangle \langle N^D \rangle + 2 \sum^6 \langle N^A \rangle \langle N^B \rangle \langle N^C \rangle \langle N^D \rangle - \sum^3 \langle N^A N^B \rangle \langle N^C N^D \rangle - 6 \langle N^A \rangle \langle N^B \rangle \langle N^C \rangle \langle N^D \rangle, \quad (3) \end{aligned}$$

where N^A denotes the number of fragments of species A (similar for B, C, D) generated in a given measurement (laser shot), and the sums are over all possible groupings of the four fragment numbers into the averages [see Eq. (A1) for the expansion of the sums].

Since the VMI apparatus measures the momentum of each fragment, the fragment numbers are functions of

momentum:

$$N^A = N(\mathbf{p}^A), \quad N^B = N(\mathbf{p}^B), \quad \text{etc.} \quad (4)$$

The fragment numbers $N(\mathbf{p})$ are stored in the computer as integers that depend on discrete values of \mathbf{p} ; their values averaged over several laser shots $\overline{N(\mathbf{p})}$ are sample frequency histograms.

While this work is focused almost exclusively on processing discrete objects, it is instructive to keep in mind their relation to the continuous population frequency distributions, which are abstract mathematical objects that can be known only with finite accuracy given finite samples. For example, the sample frequency histogram $\overline{N}(\mathbf{p})$ is related to the population frequency distribution $\mathcal{N}(\vec{\mathbf{p}})$ by the following formula:

$$\begin{aligned} \lim_{S \rightarrow \infty} \overline{N}(\mathbf{p}) &= \langle N(\mathbf{p}) \rangle \\ &= \int_{p_x-w/2}^{p_x+w/2} \int_{p_y-w/2}^{p_y+w/2} \int_{p_z-w/2}^{p_z+w/2} \mathcal{N}(\vec{\mathbf{p}}) \\ &\quad \times d\mathbf{p}_x d\mathbf{p}_y d\mathbf{p}_z, \end{aligned} \quad (5)$$

where w is the histogram bin width, and the calligraphic font denotes continuous variables. We reserve the roman font (upright, italic, and bold) for discrete variables.

When the full momentum information is used, the fragment momenta \mathbf{p} are three dimensional, which makes the terms in Eq. (3) 12-dimensional objects. This high dimensionality poses a serious computational obstacle in calculating many interesting observables (e.g., recoil frame momentum distribution, angular distribution of fragment momenta, recoil frame with respect to the laser polarization), and motivates us to seek new algorithms that overcome this difficulty. Since more than four ions are usually detected on each laser shot, we have several possible candidates for the 12-dimensional momentum quadruplets of the fragmentation process:

$$\mathbf{P}_{m_i} = [\mathbf{p}_{m_i}^A, \mathbf{p}_{m_i}^B, \mathbf{p}_{m_i}^C, \mathbf{p}_{m_i}^D]. \quad (6)$$

For example, in one given laser shot i , if we detect $N_i^A = 4$ ions of species A, $N_i^B = 2$ ions of species B, $N_i^C = 2$ ions of species C and $N_i^D = 1$ ions of species D, then there are $4 \times 2 \times 2 \times 1 = 16$ possible quadruplets \mathbf{P}_{m_i} . Here m_i is the index of the quadruplets obtained in laser shot i . These quadruplets are expansions of the term $N_i^A N_i^B N_i^C N_i^D$, which varies from shot to shot and makes the range of m_i also variable. Multiple highly charged ions may be created in the same laser shot and, unavoidably, Eq. (6) contains some false coincidence quadruplets, i.e., fragment combinations originating from different molecules, which do not represent true single-molecule Coulomb explosion events. However, the full inclusion of the subsequent 14 terms in Eq. (3), such as $\langle N^A N^B \rangle \langle N^C N^D \rangle$, effectively subtracts off these false coincidence contributions, leaving the physically meaningful correlations. Equation (3) contains $1 + 4 + 6 + 3 + 1 = 15$ different expectation values of the fragment numbers and their products, which have to be estimated from the experimental data. When constructing the estimators, denoted by a circumflex, e.g., \hat{e} , the normal procedure is to replace each expected value with the corresponding data average.

The first term, $\langle N^A N^B N^C N^D \rangle$, is different from the rest because it is composed of a simple expectation while the others are products of expectations. So for this term, the estimator is very straightforward to define and calculate in the conventional form

$$\hat{e}(\langle N^A N^B N^C N^D \rangle) = \frac{\sum_{i=1}^S N_i^A N_i^B N_i^C N_i^D}{S}, \quad (7)$$

where i denotes the index of laser shot, S is the total number of shots and N_i^A represents the number of fragments A detected in laser shot i .

Calculating observables that involve more than one fragment is often not straightforward due to the high dimensionality of Eq. (3). For example, we may want to test the momentum conservation by calculating the momentum sum: $\tilde{\mathbf{p}} = \mathbf{p}^A + \mathbf{p}^B + \mathbf{p}^C + \mathbf{p}^D$. The momentum could be 3D, or any 1D projection: this determines the dimension of the histogram.

In general, we want to construct a histogram of an observable that depends on the argument \mathbf{q} (discretized, labeling bins of the histogram) using the term $\langle N^A N^B N^C N^D \rangle$ via its estimator [Eq. (7)]. The notation is

$$\begin{aligned} \hat{e}(\langle N^A N^B N^C N^D \rangle; \mathbf{q}) &= \frac{1}{S} \sum_{i=1}^S \sum_{m_i=1}^{N_i^A N_i^B N_i^C N_i^D} \delta_w(\mathbf{q} - \mathbf{f}_q(\mathbf{P}_{m_i})), \end{aligned} \quad (8)$$

where function $\mathbf{f}_q(\mathbf{P}_{m_i})$ maps the measured instances of ion momenta \mathbf{P}_{m_i} onto the argument \mathbf{q} of the chosen observable. For example, in the case of the momentum-sum observable,

$$\mathbf{f}_q(\mathbf{P}_{m_i}) = \mathbf{p}_{m_i}^A + \mathbf{p}_{m_i}^B + \mathbf{p}_{m_i}^C + \mathbf{p}_{m_i}^D = \tilde{\mathbf{p}}_{m_i}. \quad (9)$$

An important role of the mapping function $\mathbf{f}_q(\mathbf{P}_{m_i})$ is to reduce the dimensionality of the data generated by the VMI apparatus. This is necessary because it is hard to grasp the structure of objects in the 12-dimensional space spanned by vector \mathbf{P}_{m_i} . We need an observable that is one dimensional (a plot), two dimensional (a map), or at most three dimensional (a volume map).

The finite-width δ function is defined as

$$\delta_w(\mathbf{q} - \mathbf{f}_q(\mathbf{P}_{m_i})) = \begin{cases} 1 & \text{if } \|\mathbf{q} - \mathbf{f}_q(\mathbf{P}_{m_i})\|_\infty \leq \frac{w}{2}, \\ 0 & \text{otherwise,} \end{cases} \quad (10)$$

where w is the histogram bin width, and the maximum norm, $\|\mathbf{x}\|_\infty = \max(|x_1|, |x_2|, \dots, |x_n|)$ for vector $\mathbf{x} = (x_1, x_2, \dots, x_n)$, bins the values of \mathbf{f}_q into the n -dimensional histogram of \mathbf{q} . This formulation is essentially a true or false logical function, which allows us to efficiently compute the desired histogram and extract valuable insights from the data.

Note that one can use functions other than given by Eq. (10), e.g., Gaussian kernel $g_w(\mathbf{q} - \mathbf{f}_q(\mathbf{P}_{m_i})) = e^{-\|\mathbf{q} - \mathbf{f}_q(\mathbf{P}_{m_i})\|^2/w^2} / \sqrt{\pi} w$. Different kernels have different advantages. As the experimental data from TPX3CAM are centroids of fragments [59], it is natural to use Eq. (10).

For the sake of simplicity, in the following discussion, we substitute the argument \mathbf{q} in the estimator $\hat{e}(\langle N^A N^B N^C N^D \rangle; \mathbf{q})$ with the actual observables $\tilde{\mathbf{p}}$ (momentum sum), θ (angle between two fragments' momenta), or KER (kinetic energy release). This argument has the following meanings: (1) the observable of physical interest, (2) the function that maps raw data format onto the observable, (3) the indexed observable for computer data processing purpose.

In the rest of this section we assume that the observable is one dimensional because we choose to test the conservation of $\tilde{\mathbf{p}}$ only along one coordinate \tilde{p}_x or simply \tilde{p} . To compute

the momentum sum histogram for the $\langle N^A N^B N^C N^D \rangle$ term, the following steps are required:

(1) Allocate an all-zero 1D array $H(\tilde{p})$ for a histogram of \tilde{p} .

(2) Loop through all laser shots. For a given shot i , there are $N_i^{ABCD} = N_i^A N_i^B N_i^C N_i^D$ possible four fragment quadruplets. For each quadruplet $m_i \in \{1, 2, \dots, N_i^{ABCD}\}$, we have $\tilde{p}_{m_i} = p_{m_i}^A + p_{m_i}^B + p_{m_i}^C + p_{m_i}^D$. We add 1 per event into the histogram: $H(\tilde{p}_{m_i}) = H(\tilde{p}_{m_i}) + 1$. At the end the total number of events in the histogram is $\sum_{\tilde{p}} H(\tilde{p}) = \sum_{i=1}^S N_i^A N_i^B N_i^C N_i^D$.

(3) Normalize the histogram by dividing it by the total number of shots S , yielding the momentum sum estimator for this term: $\hat{e}(\langle N^A N^B N^C N^D \rangle; \tilde{p}) = H(\tilde{p})/S$.

The sum of the normalized histogram gives us an estimate of the expected number of quadruplets in a laser shot:

$$\begin{aligned} \sum_{\tilde{p}} \hat{e}(\langle N^A N^B N^C N^D \rangle; \tilde{p}) &= \frac{\sum_{\tilde{p}} H(\tilde{p})}{S} \\ &= \frac{\sum_{i=1}^S N_i^A N_i^B N_i^C N_i^D}{S} \\ &= \hat{e}(\langle N^A N^B N^C N^D \rangle). \end{aligned} \quad (11)$$

Next, we consider the other terms of Eq. (3), which consist of multiple expectations in the cumulant formula, starting with the term $\langle N^A N^B \rangle \langle N^C N^D \rangle$ as an example. The estimator for this term can be naturally written as

$$\hat{e}(\langle N^A N^B \rangle \langle N^C N^D \rangle) = \left(\frac{1}{S} \sum_{i=1}^S N_i^A N_i^B \right) \left(\frac{1}{S} \sum_{j=1}^S N_j^C N_j^D \right). \quad (12)$$

The corresponding histogram for this term can be written as two contributions from two distinct subgroups: $\tilde{p} = (p^A + p^B) + (p^C + p^D) = p^{AB} + p^{CD}$. Because the statistics for the two subgroups are individually summed and finally collected by a product, the overall result can be computed using the idea of convolution for random variables (the advantage of using convolution over the direct method is discussed in Sec. IV; some details are relegated to the Appendix, Sec. 3). For example, in the two-body case, the histogram can be shown to be given by

$$\begin{aligned} H(\langle N^A \rangle \langle N^B \rangle; q) &= \sum_{i=1}^S \sum_{m_i=1}^{N_i^A} \sum_{j=1}^S \sum_{m_j=1}^{N_j^B} \delta_w(q - [p_{m_i}^A + p_{m_j}^B]) \\ &= \sum_{i=1}^S \sum_{m_i=1}^{N_i^A} \sum_{p^B} H(\langle N^B \rangle; p^B) \delta_w(q - [p_{m_i}^A + p^B]) \\ &= \sum_{p^A} \sum_{p^B} H(\langle N^A \rangle; p^A) H(\langle N^B \rangle; p^B) \delta_w(q - [p^A + p^B]) \\ &= H(\langle N^A \rangle; p^A) * H(\langle N^B \rangle; p^B). \end{aligned} \quad (13)$$

Here the symbol $*$ is the convolution operator of the two functions.

Substituting (A, B) with (AB, CD), we obtain

$$\begin{aligned} H(\langle N^A N^B \rangle \langle N^C N^D \rangle; \tilde{p}) &= H(\langle N^A N^B \rangle; p^{AB}) * H(\langle N^C N^D \rangle; p^{CD}), \end{aligned} \quad (14)$$

$$\begin{aligned} \hat{e}(\langle N^A N^B \rangle \langle N^C N^D \rangle; \tilde{p}) &= \frac{H(\langle N^A N^B \rangle \langle N^C N^D \rangle; \tilde{p})}{S^2} \\ &= \frac{H(\langle N^A N^B \rangle; p^{AB})}{S} * \frac{H(\langle N^C N^D \rangle; p^{CD})}{S} \\ &= \hat{e}(\langle N^A N^B \rangle; p^{AB}) * \hat{e}(\langle N^C N^D \rangle; p^{CD}). \end{aligned} \quad (15)$$

As $\hat{e}(\langle N^A N^B \rangle; p^{AB}) = H(p^A + p^B)/S$ can be computed similar to $\hat{e}(\langle N^A N^B N^C N^D \rangle; p)$, we now have a treatment for the term $\langle N^A N^B \rangle \langle N^C N^D \rangle$. It is worth noting that this treatment can be applied to any observables that are additive. For example, the momentum sum is additive in this analysis. The energy of each fragment is also additive and can give us the kinetic energy release (KER), which is an important observable.

Furthermore, because the convolution operation has associativity, we can efficiently compute the histograms for all other terms. For example,

$$\begin{aligned} \hat{e}(\langle N^A \rangle \langle N^B \rangle \langle N^C \rangle \langle N^D \rangle; \tilde{p}) &= \hat{e}(\langle N^A \rangle; p^A) * \hat{e}(\langle N^B \rangle; p^B) * \hat{e}(\langle N^C \rangle; p^C) * \hat{e}(\langle N^D \rangle; p^D), \\ \hat{e}(\langle N^A \rangle \langle N^B \rangle \langle N^C \rangle \langle N^D \rangle; \tilde{p}) &= \hat{e}(\langle N^A \rangle; p^A) * \hat{e}(\langle N^B \rangle; p^B) * \hat{e}(\langle N^C \rangle; p^C) * \hat{e}(\langle N^D \rangle; p^D). \end{aligned} \quad (16)$$

Now we have collected the histograms for each of these terms in the cumulant formula in Eq. (3) [i.e., $\hat{e}(\langle N^A N^B N^C N^D \rangle; \tilde{p})$, etc.]. We can assemble the final cumulant histogram by taking a weighted sum of them following Eq. (3):

$$\begin{aligned} \hat{e}(\varkappa_4; \tilde{p}) &= \hat{e}(\langle N^A N^B N^C N^D \rangle; \tilde{p}) \\ &- \sum_{i=1}^4 \hat{e}(\langle N^A \rangle \langle N^B N^C N^D \rangle; \tilde{p}) \\ &+ 2 \sum_{i=1}^6 \hat{e}(\langle N^A \rangle \langle N^B \rangle \langle N^C N^D \rangle; \tilde{p}) \\ &- \sum_{i=1}^3 \hat{e}(\langle N^A N^B \rangle \langle N^C N^D \rangle; \tilde{p}) \\ &- 6 \hat{e}(\langle N^A \rangle \langle N^B \rangle \langle N^C \rangle \langle N^D \rangle; \tilde{p}). \end{aligned} \quad (17)$$

The histograms of individual terms (or their permutable sums) in Eq. (17) are displayed in dashed lines in Fig. 1. As we can see from the figure, all of the terms have a broad Gaussian-like distribution, arising from false coincidences: fragment ions coming from different molecules. The first term, $\langle N^A N^B N^C N^D \rangle$, also shows a clear narrow peak around zero momentum. This is because this term captures all of the quadrupole ionization events in the same laser shot. The fragments from these true coincidence events fulfill momentum conservation, which makes the sum of their momentum to be zero. The finite width of this narrow distribution is related to the resolution of the apparatus of our instrument.

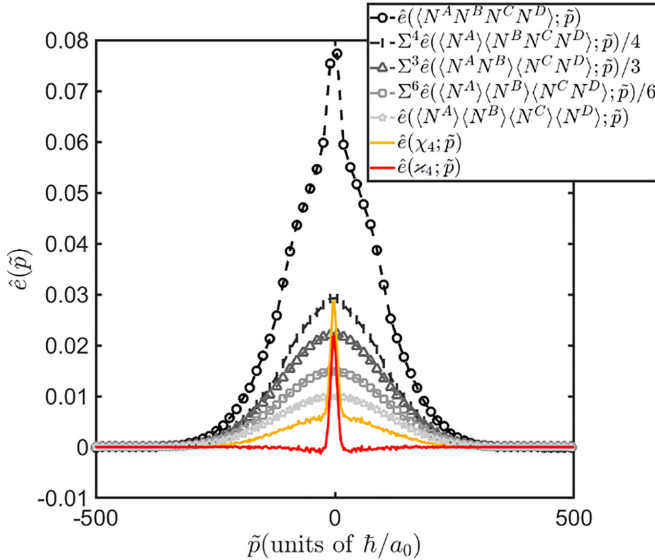


FIG. 1. Histograms of momentum sum along the x direction for four-body dissociation of CD_2O^{4+} . Five different terms (averaged by their possible permutations) that contribute to the cumulant formula in Eq. (17) are shown in dashed lines with different gray colors and markers. By adding and subtracting the other terms to the first term, we obtain fourth cumulant mapping \varkappa_4 (red solid line) and fourfold covariance mapping χ_4 (yellow solid line). The full width at half-maximum (FWHM) of the curve is about $16 \hbar/a_0$, which is close to the expected instrument response of $17 \hbar/a_0$ from an earlier analysis [61].

By following Eq. (17) to correctly subtract and add the histograms for other terms to the first term, we obtain the fourfold covariance χ_4 (yellow solid line) and 4th cumulant \varkappa_4 (red solid line) in Fig. 1. Both curves keep the narrow peak representing the true four-body coincidence but suppress the broad Gaussian-like background from false coincidences. The width of the \varkappa_4 distribution, which represents the experimental resolution of the VMI spectrometer, is much smaller than the widths of the distributions for each individual ion, as can be seen from Fig. 5 in the Appendix.

Clearly, cumulant mapping does a better job of eliminating these false coincidences than covariance mapping. We can see that the cumulant histogram is almost “background free,” with the false coincidences fully subtracted. In contrast, the covariance mapping does not get rid of these false coincidences, which come from the pairwise correlation $\sum^3 \chi_2^{AB} \chi_2^{CD}$ in Eq. (3). Details of covariance and cumulant mapping have been discussed in earlier publications [52,54].

As pointed out earlier in the text, this treatment works for histograms of any observables that are additive. This is the reason why we apply the analysis to the momentum sum. Also, for this kind of observable, a similar treatment can be applied to other covariance computations, such as twofold or threefold covariances.

It is worth noting that, aside from the narrow peak around 0, there is a shallow depression which expands $\pm 200 \hbar/a_0$ in ω_4 . We tried to identify the root of this feature. One possibility is fluctuations in the laser power. A detailed analysis of the measurements suggests that the reason is not long-term

fluctuations in the laser power, but rather shot-to-shot fluctuations in laser parameters. However, it is not clear if the laser fluctuation will give rise to the negative correlation as in this analysis, as laser fluctuation typically contributes to false-positive correlation [53,62]. Another possible origin for this weak negative signal is overlapping hits on the detector, which will interfere with the hit-finding algorithm applied in the data preprocessing. Particles with the same x - y information can suppress the count rate where the hits overlap, generating negative correlations.

In order to address these concerns or test them further, additional experimental measures could be applied. For rapid fluctuations of the laser power, one can record the pulse energy for each laser shot and feed the information into the data stream. If this is the cause of the shallow depression around 0, then extending the partial covariance technique [53,62] to the partial cumulant mapping should level the background. For the overlapping hits problem, there are many ways around it. For example, one can implement a more sophisticated hit-finding algorithm, or go to lower count rates. The former solution may slow down the data processing, while the latter may not be applicable for high-flux x-ray experiments, and requires longer time to accumulate sufficient statistics.

IV. ESTIMATING CUMULANT MAPPING OF NONADDITIVE VARIABLES

Next, we consider more complicated observables, such as the angle θ between the momenta of two particles. While the conventional estimator approach works for simpler cases, the same approach encounters difficulties with more complex observables. We take the two-body histogram as an example:

$$\begin{aligned}
& H(\langle N^A \rangle \langle N^B \rangle; \theta) \\
&= \sum_{i=1}^S \sum_{m_i=1}^{N_i^A} \sum_{j=1}^S \sum_{m_j=1}^{N_j^B} \delta_w(\theta - \cos^{-1}(\hat{\mathbf{p}}_{m_i}^A \cdot \hat{\mathbf{p}}_{m_j}^B)) \\
&= \sum_{i=1}^S \sum_{m_i=1}^{N_i^A} \sum_{\mathbf{p}^B} H(\langle N^B \rangle; \mathbf{p}^B) \delta_w(\theta - \cos^{-1}(\hat{\mathbf{p}}_{m_i}^A \cdot \hat{\mathbf{p}}^B))
\end{aligned} \tag{18a}$$

$$= \sum_{p^A} \sum_{p^B} H(\langle N^A \rangle; p^A) H(\langle N^B \rangle; p^B) \\ \times \delta_w(\theta - \cos^{-1}(\hat{p}^A \cdot \hat{p}^B)) \quad (18b)$$

$$\neq H(\langle N^A \rangle; p^A) * H(\langle N^B \rangle; p^B), \quad (18c)$$

where hats denote unit vectors, i.e., $\hat{\mathbf{p}} = \mathbf{p}/p$.

The convolution method [Eq. (18c)] cannot be applied here. Because the convolution of the two momentum histograms is the histogram of their sum momentum, rather than the angle between them, we need to go back to Eq. (18b) to calculate the product of histograms or scan all possible pairs of fragments (A, B) in Eq. (18a).

Equation (18a) is less favorable because the time taken to scan all momentum pairs is quadratic with respect to the

data size:

$$T \left(\sum_{i=1}^S \sum_{m_i=1}^{N_i^A} \sum_{j=1}^S \sum_{m_j=1}^{N_j^B} \delta_w(\theta - f_\theta) \right) \sim T \left(\sum_{i=1}^S \sum_{j=1}^S \right) \sim S^2, \quad (19)$$

where we use an abbreviation for the mapping function $f_\theta = \cos^{-1}(\hat{\mathbf{p}}_i^A \cdot \hat{\mathbf{p}}_j^B)$.

In comparison, the calculation of the product of histograms in Eq. (18b) is linear with data size. This is because the histograms of A and B are linearly dependent on the data size:

$$\begin{aligned} T &= T \left(\sum_{i=1}^S \sum_{m_i=1}^{N_i^A} \delta_w(\theta - f_\theta) \rightarrow H(\mathbf{p}^A) \right) \\ &\quad + T \left(\sum_{j=1}^S \sum_{m_j=1}^{N_j^B} \delta_w(\theta - f_\theta) \rightarrow H(\mathbf{p}^B) \right) \\ &\quad + T \left(\sum_{\mathbf{p}^A} \sum_{\mathbf{p}^B} H(\mathbf{p}^A) H(\mathbf{p}^B) \delta_w(\theta - f_\theta) \right) \\ &= O(S) + O(S) + O(L^2). \end{aligned} \quad (20)$$

Here L is the number of bins for $H(\mathbf{p})$. In this method, the last step may take significant time to compute despite having to be done only once. Similar to Eq. (18a), where one needs to scan all cases of fragments (A, B), Eq. (18b) now requires scanning all momentum pairs $(\mathbf{p}^A, \mathbf{p}^B)$. For a 3D camera, each of the momentum dimensions would have >100 bins, resulting a 3D histogram of $L > 100^3 = 10^6$ bins. Thus, the momentum pair has dimension of $L^2 > 10^6 \times 10^6 = 10^{12}$. Clearly, the computation timescales nonlinearly with the number of particles involved. Four particle correlations would require computation on the order of $L^4 > (10^6)^4 = 10^{24}$. Such a large number of calculations is not feasible on normal computers and poses a serious challenge in the data analysis.

Note that the convolution operation $f * g$ normally costs $O(L^2)$ calculations. Essentially, the convolution method in Eq. (18c) is identical to the product of histograms in Eq. (18b). But, in principle, one can benefit from the well-developed fast Fourier transform (FFT) algorithm to speed up its calculation:

$$f * g = \text{FFT}^{-1}[\text{FFT}(f) \cdot \text{FFT}(g)]. \quad (21)$$

Since the FFT algorithm has been demonstrated to perform as fast as $O(L \ln L)$, the above computation can be completed in $T_{\text{FFT}}(f * g) = O(L \ln L) + O(L \ln L) + O(L) + O(L \ln L) = O(L \ln L)$. With this observation, the product of histograms in Eq. (18b) can be much faster if it can be computed in a different way, but this increase in computational speed may not apply to all observables.

Given the excessive computational requirements of the conventional estimator, it is necessary to explore alternative computational strategies. We have investigated different forms of the conventional estimator [Eq. (18a)] in search of a solution. However, an intrinsic problem arises when attempting to estimate both $\langle N^A N^B \rangle$ and $\langle N^C N^D \rangle$ accurately, which are

required for the calculation of $\langle N^A N^B \rangle \langle N^C N^D \rangle$. One needs to estimate both terms precisely in order to have a good estimation of their product. Details can be found in the Appendix, Sec. 9.

Now let us reconsider the product of expectation values. To correctly estimate this, we need to make sure that the two sets of fragments are coming from independent events, which is usually achieved by considering pairs of fragments from different laser shots. This means that we could force the two sets of fragments to have different laser shot indices. This realization motivates a different solution: while looping over the index for fragments (A, B) $\sum_{i=1}^S N_i^A N_i^B$, one can also add (C, D) $N_j^C N_j^D$ by using a separate index j that is different from i . This guarantees the independence of (A, B) to (C, D) but allows the calculation to be performed more efficiently. Based on this reasoning, we introduce the following estimator:

$$\hat{e}^{\text{new}}(\langle N^A N^B \rangle \langle N^C N^D \rangle) = \frac{1}{S} \sum_{i=1}^S N_i^A N_i^B N_{i+\alpha}^C N_{i+\alpha}^D. \quad (22)$$

Here α is a fixed number that offsets the looping indices of the two sets of fragments. From the discussion above, it is clear that our estimator converges to the desired estimand:

$$\begin{aligned} \langle \hat{e}^{\text{new}}(\langle N^A N^B \rangle \langle N^C N^D \rangle) \rangle &= \frac{1}{S} \sum_{i=1}^S \langle N_i^A N_i^B N_{i+\alpha}^C N_{i+\alpha}^D \rangle \\ &= \frac{1}{S} \sum_{i=1}^S \langle N_i^A N_i^B \rangle \langle N_{i+\alpha}^C N_{i+\alpha}^D \rangle \\ &= \langle N^A N^B \rangle \langle N^C N^D \rangle. \end{aligned} \quad (23)$$

The computation time spent on this estimator is linear with respect to the data size (number of laser shots), regardless of which term is computed:

$$\begin{aligned} T(\hat{e}^{\text{new}}(\langle N^A N^B \rangle \langle N^C N^D \rangle)) &\approx \sum_{i=1}^S N_i^A N_i^B N_{i+\alpha}^C N_{i+\alpha}^D \\ &\approx S \langle N^A N^B \rangle \langle N^C N^D \rangle \propto S, \\ T(\hat{e}^{\text{new}}(\langle N^A \rangle \langle N^B \rangle \langle N^C \rangle \langle N^D \rangle)) &\approx \sum_{i=1}^S N_i^A N_{i+\alpha}^B N_{i+\beta}^C N_{i+\gamma}^D \\ &\approx S \langle N^A \rangle \langle N^B \rangle \langle N^C \rangle \langle N^D \rangle \propto S. \end{aligned} \quad (24)$$

The second case in the above equation is a multiplication of four expectation values. In this case, by utilizing more offset parameters α, β, γ , which are not equal to each other, we ensure that the fragments come from independent events.

To assess the usefulness of this estimator, we should examine the achievable signal-to-noise ratio for the calculated cumulant. One can compute the variance, from which the signal to noise is given by $S/N = \frac{\langle \hat{e} \rangle}{\sqrt{\text{var}(\hat{e})}}$. Both the conventional and the new estimator have the same expectation value. The

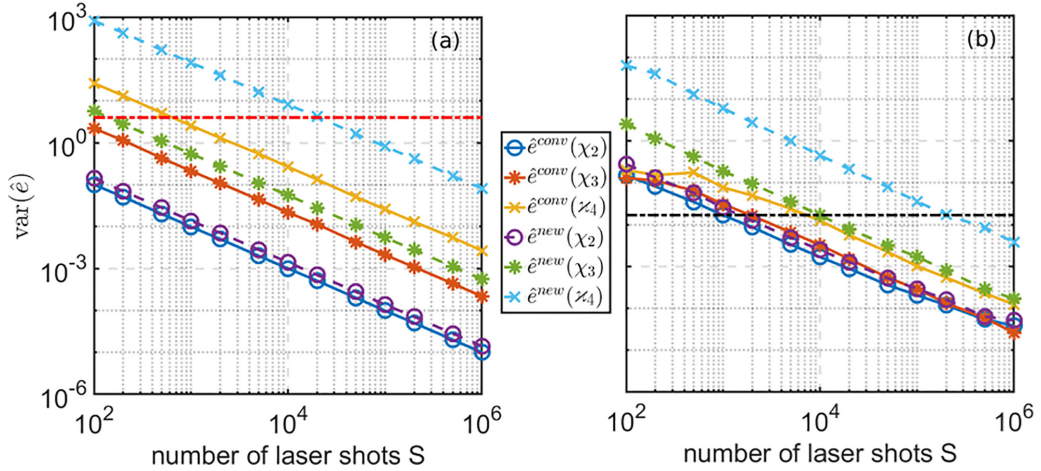


FIG. 2. The variance for conventional estimator [solid lines, represented by Eq. (12)] and new estimator [dashed lines, represented by Eq. (22)] as a function of the number of laser shots S for simulated data (a) and experimental data (b). Three orders of cumulants χ_2 (o), χ_3 (*), and χ_4 (x) are shown in the plot. Note that all of the lines have a slope of -1 on the log-log plot, meaning that the estimator converges with increasing number of laser shots at rate of S^{-1} . For reference, all lines in panel (a) have the same expectation value by design: $\langle \hat{e} \rangle = 2$. The red dashed line marks $S/N = 1$. The experimental data analyzed in (b) involve many dissociation channels and the mean value for fourfold channel at $S = 10^6$ is $\bar{e}(\chi_4) = 0.13$. The black dashed line marks where the variance of the two estimators $\text{var}(\hat{e}(\chi_4))$ reach $S/N = 1$.

only challenge is the computation of the variance since the calculation of $\text{var}(\hat{e})$ is not trivial.

Although it would be ideal to estimate the S/N ratio of χ_4 as a function of S , it is almost impossible to compute the analytical expression of its variance because there are in principle more than 100 covariance terms from the variance of 15 terms in Eq. (3). Fortunately, detailed calculations have been carried out to estimate the variance of the conventional estimator [54]. This work involves many complicated products of expectations. But with some simple approximations, additional experimental complexities can be factorized (e.g., detection efficiency and background event rate, etc.). Additionally, we run simple simulations to sample the same Poisson distribution multiple times. By computing both estimators for the simulated data, we obtain many instances of the cumulants through these estimators, and thus simulate the variance of the estimator. A similar analysis can be performed on the experimental data. The details of the analysis can be found in the Appendix, Secs. 7 and 8.

Figure 2 shows a log-log plot of the variance as a function of the number of shots S . Different covariance orders χ_2 (o), χ_3 (*), and χ_4 (x) are computed using the conventional estimator [solid line, represented by Eq. (12)] and our estimator [dashed line, represented by Eq. (22)]. The analysis in Fig. 2(a) is performed on a simulated data set. From the plot, we can see that all of these variances have the same slope in the log-log plot. This means that the estimator's variance converges with increasing laser shots at rate of S^{-1} . Clearly, both the conventional estimators and the new estimators show the same trend. Even though S^n computations are involved in the conventional estimator, many of them are not independent from each other. In fact, there are S unique laser shots (independent measurements) and that is why the variance of the conventional estimators also scales as the new estimators, which also involve S unique laser shots. Aside from the same trend over S , there is a gap in performance between the con-

ventional estimator and the new estimator for each order of covariance. This is the price that we pay for not performing all of the S^n calculations. For two- and three-body correlation, the gaps between the two estimators are not significant, but the fourth cumulant would benefit from a better implementation of the algorithm.

Figure 2(b) depicts the same S dependence of different estimators from the experimental correlations: $\chi_2(D^+, D^+)(o)$, $\chi_2(D^+, D^+, O^+)(*),$ and $\chi_4(D^+, D^+, O^+, C^+)(x)$. Due to the practical limitations, we cannot run the same experiments 2000 times while keeping all of the experimental conditions identical, as assumed in the simulated data. Thus, the errors on estimating these variances are larger than in Fig. 2(a) but there is qualitative agreement between the two panels. Similar to Fig. 2(a), all of the variances converge with increasing laser shots at the rate of S^{-1} . Regardless of significant differences in the vertical positions of the lines, the new estimators have larger variance than the conventional estimators, resulting in a smaller S/N ratio, which favors the conventional estimator if computational time were not an issue. However, the calculation of the distributions of complicated observables using the conventional estimator often requires excessive computational time.

We want to compare the simulations to the experimental data. The simulated data have only one dissociation channel, which has the expected number of events per shot $\langle \hat{e} \rangle = 2$. As a result, all of the estimators in Fig. 2(a) reach $S/N = 1$ when $\text{var}(\hat{e}) = \langle \hat{e} \rangle^2 = 4$ (red dashed line). Most of the estimators can reach this level by $S = 10^4$ shots, which is suitable for a 1-kHz laser system. The required number of shots to reach a certain S/N ratio depends on the counting rate of events. Moreover, in the real experiments the events usually comprise of multiple dissociation channels and their relative yields are typically unknown in advance. To overcome these complications, we use the measured four-body event rate at $S = 10^6$, which is $\bar{e}(\chi_4) = 0.13$. The variance of the two estimators

TABLE I. Variance of simulated (this work) and theoretical [54] cumulants at a single shot producing on average 2 ions of each kind, detected with 100% quantum efficiency and containing no background ions.

Variance of	Simulation	Theory
$\hat{e}(\chi_2)$	10	10
$\hat{e}(\chi_3)$	120	218
$\hat{e}(\chi_4)$	2300	2666

$\text{var}(\hat{e}^{\text{conv}}(\chi_4))$ and $\text{var}(\hat{e}^{\text{new}}(\chi_4))$ approach $S/N = 1$ [black dashed line in Fig. 2(b)] around $S = 10^4$ and $S = 2 \times 10^5$, respectively. So far, this analysis is performed at a single point on the cumulant map rather than a range of points, which is discussed in the next section. Further discussions of the S/N ratio can be found in [54–56].

In addition to comparing the simulations to real experiments, we also compare them to the theoretical predictions of the single-shot variance [54]. The single-shot variance in the simulation is obtained by rescaling the variance to $S = 1$ (see Table I).

As expected, the theory overestimates the variance of the third and higher cumulants because it approximates some of the sample averages by the expected values [Eq. (35) in [54]]. These estimations provide valuable insights into the computational efficiency and accuracy of our estimator in practical scenarios.

Note that, with the increasing number of fragments in the system, the variance of the correlation (covariance or cumulant) is increasing by almost a factor of 10 with each additional fragment. This implies that the S/N ratio significantly worsens as we increase the number of fragments in the correlation.

V. PERFORMANCE OF THE ALGORITHM IN A MOMENTUM CONSERVATION STUDY

Next, we aim to see if real experiments could produce a signal-to-noise ratio similar to the simulations. First, we outline the algorithm for our estimator of total momentum:

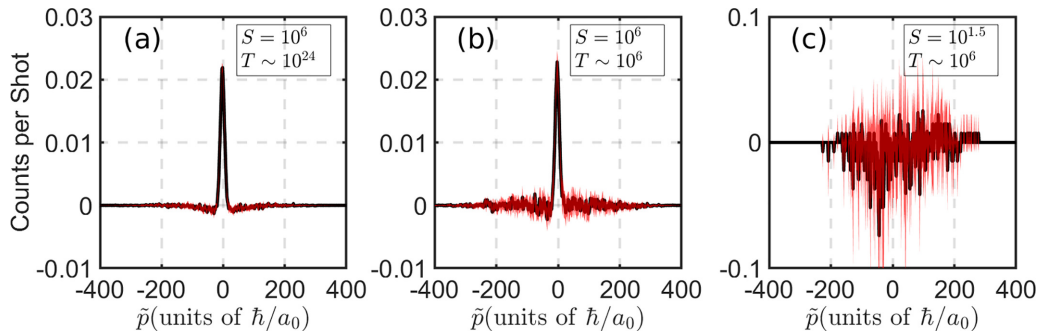


FIG. 3. Comparison of the performance of the two algorithms in constructing a histogram of momentum conservation using the fourth cumulant. (a) The cumulant mapping calculated using the conventional estimator $\hat{e}^{\text{conv}}(\chi_4)$ with a total of $S = 1.2 \times 10^6$ shots. The 95% confidence region is shaded in red. (b) The same cumulant calculated using the new estimator $\hat{e}^{\text{new}}(\chi_4)$ using total $S = 1.2 \times 10^6$ shots. (c) The same cumulant calculated using the conventional estimator $\hat{e}^{\text{conv}}(\chi_4)$ with a total of $S = 33$ shots, making use of the same computational time as used in calculating (b); note the change in the vertical scale and that the momentum-conservation peak is buried in the noise. The new estimator clearly achieves a better S/N ratio than the conventional estimator when using the same computational time.

(1) For any cumulant term, e.g., $\langle N^A N^B \rangle \langle N^C N^D \rangle$, we loop over laser shots. For a given shot i , there are $N_{i,i+1}^{\text{ABCD}} = N_i^A N_i^B N_{i+1}^C N_{i+1}^D$ possible quadruplets. We choose the index offset α , to be 1, as an example. Thus, in total, there are $\sum_{i=1}^S N_i^A N_i^B N_{i+1}^C N_{i+1}^D$ quadruplets. We allocate a 2D array \mathbf{G} of size (number of quadruplets) \times (number of momentum coordinates) $= (\sum_{i=1}^S N_i^A N_i^B N_{i+1}^C N_{i+1}^D) \times 12$ in memory.

(2) In a given shot, we loop through all these possible quadruplets. For each quadruplet $j \in \{1, 2, \dots, N_{i,i+1}^{\text{ABCD}}\}$, we store the quadruplet momentum information \mathbf{P} in array \mathbf{G} . We do the same at the next trigger, etc., until we collect all $(\sum_{i=1}^S N_i^A N_i^B N_{i+1}^C N_{i+1}^D) \times 12$ quadruplets in \mathbf{G} .

(3) We repeat the above operation for all other cumulant terms. Each of them has its own 12-column \mathbf{G} array; there are 15 such arrays.

(4) Then we construct the histogram of the momentum sum. We compute the new array $\tilde{\mathbf{G}}$, by summing the ion momenta in each element in array \mathbf{G} : $\tilde{p}_{m_i} = p_{m_i}^A + p_{m_i}^B + p_{m_i}^C + p_{m_i}^D$. We store all these momenta for further analysis and repeat this process for all 15 terms.

(5) We bin the $\tilde{\mathbf{G}}$ array into 15 histograms, such as $\hat{e}(\langle N^A N^B \rangle \langle N^C N^D \rangle; \tilde{p})$, which are the estimators given by Eq. (24).

(6) Finally, we use Eq. (3) to sum the 15 histograms into the fourth cumulant mapping:

$$\begin{aligned} \hat{e}(\chi_4; \tilde{p}) = & \hat{e}(\langle N^A N^B N^C N^D \rangle; \tilde{p}) \\ & - \sum^4 \hat{e}(\langle N^A \rangle \langle N^B N^C N^D \rangle; \tilde{p}) \\ & + 2 \sum^6 \hat{e}(\langle N^A \rangle \langle N^B \rangle \langle N^C N^D \rangle; \tilde{p}) \\ & - \sum^3 \hat{e}(\langle N^A N^B \rangle \langle N^C N^D \rangle; \tilde{p}) \\ & - 6 \hat{e}(\langle N^A \rangle \langle N^B \rangle \langle N^C \rangle \langle N^D \rangle; \tilde{p}). \end{aligned} \quad (25)$$

Note that our algorithm is general, meaning that it can handle any observables, including the calculation in the recoil frame of the ejection angle between any two fragments [52].

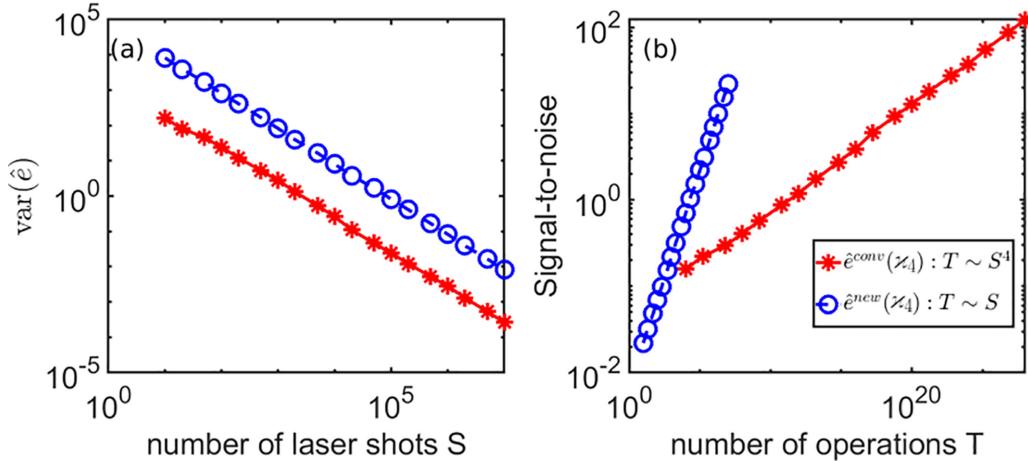


FIG. 4. (a) Dependence of variance of cumulant estimators on the number of laser shots. The curves that utilize the conventional (red circles) and new estimators (blue circles) show the same S^{-1} trend. (b) Shows the correlation between signal-to-noise ratio $S/N = \frac{\langle \hat{e} \rangle}{\sqrt{\text{var}(\hat{e})}}$ and estimated computation time T (in units of number of computation operations) using different estimators. The computation time reflects the simple power-law dependence $T \sim S^n$, where the power index n is 4 for the fourth cumulant's conventional estimator and 1 for the new estimator.

Figure 3 compares the computational performance of our algorithm to the conventional one, by constructing a histogram of total momentum. Figures 3(a) and 3(c) utilize the conventional estimator and Fig. 3(b) uses the new estimator. The narrow peak in each panel is due to momentum conservation. The presence of this peak in Fig. 3(a) validates the convolution method. In Fig. 3(b) this peak demonstrates that it is correct to directly estimate the product $\langle N^A \rangle \langle N^B \rangle$, rather than the two factors separately.

The experimental variance is also computed for each of the estimators by chopping the full data set into smaller pieces, computing histograms of momentum sum on each of the pieces, and analyzing the variance among all pieces. The red shaded area in all panels of Fig. 3 shows the 95% confidence level. We can clearly see that, if we ignore the difference in computational time of the two estimators, the noise level of the conventional estimator in Fig. 3(a) is significantly lower than that of the new estimator in Fig. 3(b). While the signals are the same, the signal-to-noise ratio of our method is worse. This behavior is expected because we have a significant decrease in the computational time $T(\hat{e}^{\text{new}})$, at the expense of the signal-to-noise ratio.

Next, we compare the two estimators when considering the computational time for complicated observables. Since the computational time of the two estimators scales differently with the number of shots [compare Eqs. (1) and (24)], in the time the new estimator processes S shots, the conventional estimator can only process approximately $\sqrt[4]{S}$ shots, which for the analysis shown in Fig. 3(b) is only $S = \sqrt[4]{10^6} \approx 33$ shots. Consequently, the signal is completely overwhelmed by the noise, as shown in Fig. 3(c). Thus, given a similar computational time, the new estimator achieves a much better signal-to-noise ratio than the conventional estimator.

This demonstrates the computational efficiency of our estimator and its ability to strike a balance between computational time and signal fidelity. The essence of this estimator is to select certain subsets of the full sums present in the conven-

tional estimator. In the future, we hope to further optimize the formulation of our estimator to reduce the noise in Fig. 3(b) closer to the ideal case of Fig. 3(a), while keeping a manageable computational time.

In order to explore potential improvements and search for a better estimator, we compare the variance of the two methods using simple simulations. This allows us to evaluate the signal-to-noise ratio under different parameter settings, e.g., counting rates of different channels. Such an evaluation gives us a quantitative assessment of the improved estimator, which should keep $T \sim S$ but reduce the signal-to-noise ratio close to the ideal case. Also, it is much easier to explore the parameter space by running the simulations rather than real experiments.

The results of the simulations are shown in Fig. 4(a). We can see that the variances of both the conventional estimator (red) and the new estimator (blue) follow the same S^{-1} dependence as seen in Fig. 2. And the ratio of the two lines is approximately 30, which means that the new estimator needs roughly 30 times more laser shots to reach the same signal-to-noise ratio. This also means that the signal-to-noise ratio is about 5.5 times lower for the new estimator than the conventional one, which is consistent with Fig. 3. It is important to note, however, that this comparison does not take the computation time into account.

Figure 4(b) presents the signal-to-noise ratio of the two methods with respect to their computation time. The signal-to-noise ratio $S/N = \frac{\langle \hat{e} \rangle}{\sqrt{\text{var}(\hat{e})}}$ is obtained from the simulation of the variance by varying the number of shots, similar to Fig. 4(a). The computation time for different estimators is assumed to have the simple relationship: $T = S^n$, where the power index n is given by the largest number of nested loops that scan the laser shots in a given estimator. While there may be a prefactor in this formula, it has been neglected for simplicity. Clearly, from Fig. 4(b), we can see that even though the conventional estimator has better signal-to-noise values, the time needed to perform the full computation is orders of magnitude larger than for the new estimator. This finding

highlights our estimator's ability to find a favorable compromise between signal-to-noise ratio and computation time.

Overall, the comprehensive analysis presented in Fig. 4 highlights the computational efficiency of our estimator. It shows the tradeoff between computational time and signal-to-noise ratio and emphasizes the potential for further refinements in our estimator's formulation to achieve an optimal balance between these characteristics.

Some improvements to our estimator seem to be possible. For example, by changing the parameter α to other than $\alpha = 1$, the algorithm may perform better. Especially, in free-electron laser (FEL) facility, there may be correlation between adjacent x-ray pulses. Assigning a different parameter α can avoid this problem. Also, one can try two (or more) parameters α_1 and α_2 , to calculate $\hat{\epsilon}^{\text{new}} = \frac{1}{2S} \sum_{i=1}^S N_i^A N_i^B (N_{i+\alpha_1}^C N_{i+\alpha_1}^D + N_{i+\alpha_2}^C N_{i+\alpha_2}^D)$. This estimator takes a little more time to compute but still stays within $T \sim S$ computation time.

We note that this signal-to-noise simulation is carried out only for a single point on a cumulant map. In a real experiment, we normally study a region of the map, such as $\hat{\epsilon}(\varkappa_4(\vec{p}))$. By performing momentum gating on the momentum-conserved events, e.g., (D^+, D^+, C^+, O^+) in the strong-field ionization of CD_2O , one can remove an obvious background and obtain a better signal-to-noise ratio.

VI. CONCLUSION

In conclusion, we have introduced an algorithm for computing cumulant maps, covering both additive and more complex observables. While this algorithm may not achieve as good a signal-to-noise ratio as the approach based on the conventional estimator, its remarkable computational speed far surpasses that of the conventional method. This computational efficiency is of great importance in handling high count rates, and allows for the analysis of a broader range of observables. Moreover, the versatility of this algorithm extends beyond Coulomb explosion studies and can be applied to various research areas requiring the analysis of correlated particle emission.

Future efforts will focus on refining the balance between the signal-to-noise ratio and computation time, aiming to optimize the performance of cumulant mapping. This involves exploring the exact form of our estimator. By continuously improving the algorithm and incorporating advanced computational techniques, we can gain deeper insights into the dynamics of complex systems and ultrafast science. Overall, cumulant mapping provides a valuable framework for investigating ultrafast processes and has the potential to revolutionize our understanding of correlated particle emission. With its computational efficiency and flexibility in handling diverse observables, this approach opens up different avenues for studying complex phenomena in ultrafast science.

ACKNOWLEDGMENTS

R.F. and F.A. acknowledges support from the Linac Coherent Light Source, SLAC National Accelerator Laboratory, which is supported by the U.S. Department of Energy, Office of Science, Office of Basic Energy Sciences, under Contract No. DE-AC02-76SF00515. C.C. and A.J.H. were supported by the National Science Foundation. A.J.H. was additionally supported under a Stanford Graduate Fellowship as the 2019 Albion Walter Hewlett Fellow. C.C., G.M., and T.W. acknowledge support from the U.S. Department of Energy under Award No. DE-FG02-08ER15984. The authors thank T. Driver (SLAC National Accelerator Laboratory), D. Rolles (Kansas State University), and M. Brouard (University of Oxford) for fruitful discussions and for helping to facilitate this research collaboration.

C.C. came up with the original research idea and the algorithm. C.C. and G.M. performed the experiment. L.J.F. described the algorithm in terms of mathematical formalism. G.M., F.A., A.J.H., P.H.B., R.F. and T.W. helped in discussion and writing of the manuscript.

APPENDIX

1. Expansion of the four-body cumulant formula

The sums in Eq. (3) should be expanded as follows:

$$\begin{aligned}
 \varkappa_4 &= \langle N^A N^B N^C N^D \rangle - \sum^4 \langle N^A \rangle \langle N^B N^C N^D \rangle + 2 \sum^6 \langle N^A \rangle \langle N^B \rangle \langle N^C N^D \rangle - \sum^3 \langle N^A N^B \rangle \langle N^C N^D \rangle - 6 \langle N^A \rangle \langle N^B \rangle \langle N^C \rangle \langle N^D \rangle \\
 &= \langle N^A N^B N^C N^D \rangle - (\langle N^A \rangle \langle N^B N^C N^D \rangle + \langle N^B \rangle \langle N^A N^C N^D \rangle + \langle N^C \rangle \langle N^A N^B N^D \rangle + \langle N^D \rangle \langle N^A N^B N^C \rangle) \\
 &\quad + 2(\langle N^A \rangle \langle N^B \rangle \langle N^C N^D \rangle + \langle N^A \rangle \langle N^C \rangle \langle N^B N^D \rangle + \langle N^A \rangle \langle N^D \rangle \langle N^B N^C \rangle + \langle N^B \rangle \langle N^C \rangle \langle N^A N^D \rangle + \langle N^B \rangle \langle N^D \rangle \langle N^A N^C \rangle) \\
 &\quad + \langle N^C \rangle \langle N^D \rangle \langle N^A N^B \rangle - (\langle N^A N^B \rangle \langle N^C N^D \rangle + \langle N^A N^C \rangle \langle N^B N^D \rangle + \langle N^A N^D \rangle \langle N^B N^C \rangle) - 6 \langle N^A \rangle \langle N^B \rangle \langle N^C \rangle \langle N^D \rangle. \quad (A1)
 \end{aligned}$$

2. Camera image processing

The VMI ion data from TPX3CAM consist of binary images of ion hits. Typically, there are 10 to 20 hits per shot forming dots in the image. Additionally to the position of an image pixel, its time-of-arrival information is also recorded if the intensity exceeds a certain threshold, which is set to have negligible dark counts. Since the dots vary in size and

intensity, a centroiding algorithm is employed and the time-of-arrival is corrected to obtain each ion's x, y, t coordinates [59]. Finally, a ToF analysis identifies the species of each of the fragments.

In general, a time-stamping optical camera, or a wire-grid anode array, records complete momentum information for every ion detected after

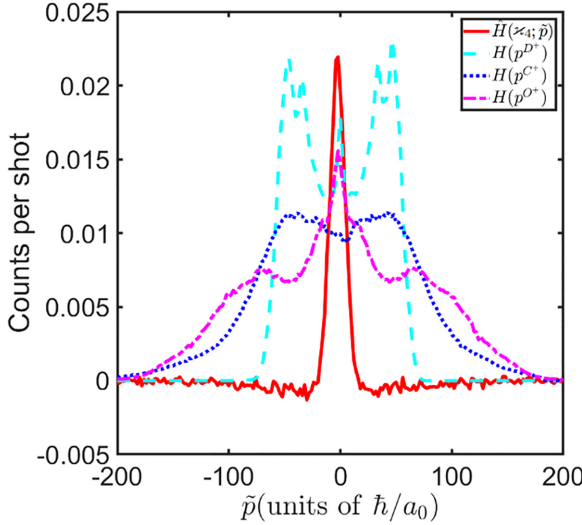


FIG. 5. Momentum distributions of D^+ (light dashed line), C^+ (dark blue dotted line), O^+ , or CD_2^+ (purple dashed-dotted line) ions along the laser polarization direction x . Each distribution is normalized such that their sum is 1. All of them have much broader distribution than the fourth cumulant \varkappa_4 (red solid line) of the correlated channel: (D^+ , D^+ , C^+ , O^+).

centroiding:

$$\begin{aligned} \mathbf{p} &= [p_x, p_y, p_z] = F(x, y, t) \\ &= [C(x - x_0), C(y - y_0), C'(t - t_0)], \end{aligned} \quad (A2)$$

where the ion momentum vector \mathbf{p} is measured in the laboratory frame, which has the x axis aligned with the laser E field, and the p_z momentum component is derived from the ion time of flight t , using an instrument calibration function F . For the case of TPX3CAM and the VMI apparatus that we are using, the calibration is roughly linear in all three dimensions. The x and y dimensions have the same coefficient C and the z dimension has a different coefficient C' , found from the ToF analysis.

3. Convolution in terms of the delta function

For any functions f, g , their convolution is given by

$$\begin{aligned} \sum_{x,y} f(x)g(y)\delta_w(z - [x + y]) &= \sum_x f(x)g(z - x) \\ &= \{f * g\}(z), \end{aligned} \quad (A3)$$

where δ_w is the finite-width δ function defined by Eq. (10).

This relationship can be extended to three or more functions:

$$\begin{aligned} \sum_{x,y,z} f(x)g(y)h(z)\delta_w(v - [x + y + z]) &= \sum_{x,y} f(x)g(y)h(v - x - y) \\ &= \sum_x f(x)\{g * h\}(v - x) \\ &= \{f * \{g * h\}\}(v) \\ &= \{f * g * h\}(v). \end{aligned} \quad (A4)$$

4. Fragment's momentum distribution along laser polarization

Figure 5 shows ion momentum distributions along the laser polarization x . Plots for different ions are labeled by different markers. The momentum sum given by the fourth cumulant \varkappa_4 is plotted in red. As clearly can be seen from these plots, all the individual ion distributions are much broader than their correlated cumulant \varkappa_4 . The FWHM of the cumulant central peak is $16 \hbar/a_0$, while the detector response function propagated through the momentum-conservation formula gives $17 \hbar/a_0$. It seems that our analysis is limited only by the experimental resolution.

5. List of symbols

Symbol	Meaning
n	order of nonlinearity or number of particles
\varkappa_n	n^{th} -order cumulant
χ_n	n^{th} -order covariance
T	computational time or time complexity of an estimator
S	number of laser shots in a sample
i, j, k	laser shot indices in a sample
A, B, C, D	a quadruple of the parent molecule fragments
N_i^A	number of fragments A in laser shot i
\bar{N}^A	average value of N^A in a sample
$\langle N^A \rangle$	expected value of N^A
$\hat{e}(\langle N^A \rangle)$	estimator of $\langle N^A \rangle$ such that $\langle \hat{e}(\langle N^A \rangle) \rangle = \langle N^A \rangle$
$\text{var}(\hat{e})$	variance of an estimator
m_i	index of a quadruple in laser shot i
$\mathbf{P}_{m_i}^A$	3D momentum of fragment A in quadruple m_i
\mathbf{P}_{m_i}	12D momentum vector of quadruple m_i
$\tilde{\mathbf{P}}_{m_i}$	sum of fragment momenta for quadruple m_i
\mathbf{q}	argument of an observable derived from \mathbf{P}
$\hat{e}(\langle N^A \rangle; \mathbf{q})$	estimator of $\langle N^A \rangle$ resolved for observable \mathbf{q}
$f_{\mathbf{q}}(\mathbf{P}_{m_i})$	function mapping momentum \mathbf{P}_{m_i} to observable \mathbf{q}
$\delta_w(\mathbf{q} - f_{\mathbf{q}})$	δ -function of width w that bins $f_{\mathbf{q}}$ values into an array of \mathbf{q}
$H(\varkappa_4; \tilde{p})$	1D histogram of \varkappa_4 as the function of momentum sum

6. Estimator choice for different observables

There are three cases that lead to different estimators. First, if an observable is not derived from a particular species, then the covariance or cumulant estimator benefits from keeping nested expectation values for this species. For example, if we are interested in cumulant mapping of three species A, B and C , where C is only needed for its counts, then the histogram of the third cumulant can be calculated as follows:

$$\begin{aligned} H(\chi_3^{\text{ABC}}; \mathbf{q}^{\text{AB}}) &= H(\langle (N^A - \langle N^A \rangle)(N^B - \langle N^B \rangle)(N^C - \langle N^C \rangle) \rangle; \mathbf{q}^{\text{AB}}) \\ &= \sum_{i=1}^S H(\langle (N_i^A - \langle N^A \rangle)(N_i^B - \langle N^B \rangle) \rangle; \mathbf{q}^{\text{AB}})(N_i^C - \langle N^C \rangle) \\ &= \sum_{i=1}^S H(\langle (N_i^A - \langle N^A \rangle)(N_i^B - \langle N^B \rangle) \rangle; \mathbf{q}^{\text{AB}}) N_i^C. \end{aligned} \quad (A5)$$

Effectively, particle C enters the formula only as the weight $N_i^C = N_i^C - \langle N^C \rangle$ and reduces the complexity of the computation in the higher-fold channels, regardless of how complicated the observable \mathbf{q}^{AB} is:

$$\delta_w(\mathbf{q}^{AB} - f_{\mathbf{q}}(p_i^A, p_j^B)) \longrightarrow \delta_w(\mathbf{q}^{AB} - f_{\mathbf{q}}(p_i^A, p_j^B)) N_k^C. \quad (\text{A6})$$

The second case is when the observable is additive, which we have discussed in the context of momentum conservation. In this case, the convolution helps to compute the histogram of the product of the expectation values:

$$\begin{aligned} H(\langle N^A \rangle \langle N^B \rangle; p^{AB}) &= \sum_{i=1}^S \sum_{m_i=1}^{N_i^A} \sum_{j=1}^S \sum_{m_j=1}^{N_j^B} \delta_w(p - [p_{m_i}^A + p_{m_j}^B]) \\ &= H(\langle N^A \rangle; p^A) * H(\langle N^B \rangle; p^B). \end{aligned} \quad (\text{A7})$$

The momentum sum and KER sum are clearly such kinds of additive observables that can benefit from this method.

Observables that depend only on one coordinate can be also calculated efficiently. For example in the ToF-ToF histogram, the noncoincidence term can be factorized:

$$\begin{aligned} &H(\langle N^A \rangle \langle N^B \rangle; t_1, t_2) \\ &= \sum_{i=1}^S \sum_{m_i=1}^{N_i^A} \sum_{j=1}^S \sum_{m_j=1}^{N_j^B} \delta_w(t_1 - t_{m_i}^A, t_2 - t_{m_j}^B) \\ &= \sum_{i=1}^S \sum_{m_i=1}^{N_i^A} \sum_{j=1}^S \sum_{m_j=1}^{N_j^B} \delta_w(t_1 - t_{m_i}^A) \delta_w(t_2 - t_{m_j}^B) \\ &= \sum_{i=1}^S \sum_{m_i=1}^{N_i^A} \delta_w(t_1 - t_{m_i}^A) \sum_{j=1}^S \sum_{m_j=1}^{N_j^B} \delta_w(t_2 - t_{m_j}^B) \\ &= H(\langle N^A \rangle; t_1) H(\langle N^B \rangle; t_2), \end{aligned} \quad (\text{A8})$$

where $H(\langle N^A \rangle \langle N^B \rangle; t_1, t_2)$ is the 2D histogram and $H(\langle N \rangle; t)$ are 1D histograms. Since t_1 and t_2 are on different axes, the 1D histograms can be calculated by scanning the shots only once, and subsequently the 2D histogram can be obtained as an outer product of the two 1D vectors.

We can extend this formula to look at the correlation of more particles, for example,

$$\begin{aligned} &H(\langle N^A \rangle \langle N^B \rangle \langle N^C \rangle \langle N^D \rangle; t_1, t_2, t_3, t_4) \\ &= H(\langle N^A \rangle; t_1) H(\langle N^B \rangle; t_2) H(\langle N^C \rangle; t_3) H(\langle N^D \rangle; t_4). \end{aligned} \quad (\text{A9})$$

The increased dimensionality of this histogram, however, may cause problems with computer storage and interpretation of multidimensional features. The dimensionality can be reduced for additive observables, such as momentum (see Sec. III), where we can construct $H(t^A + t^B, t^C + t^D)$ or $H(t^A, t^B + t^C + t^D)$.

The most difficult case is when the observable depends on two or more coordinates in a nonlinear way. One example is

the angle between two fragments' momenta:

$$\begin{aligned} &H(\langle N^A \rangle \langle N^B \rangle; \theta) \\ &= \sum_{i=1}^S \sum_{m_i=1}^{N_i^A} \sum_{j=1}^S \sum_{m_j=1}^{N_j^B} \delta_w(\theta - \cos^{-1}(\hat{p}_{m_i}^A \cdot \hat{p}_{m_j}^B)). \end{aligned} \quad (\text{A10})$$

In Sec. IV, we have discussed this case in detail and proposed an estimator that can be calculated fast but at the expense of increased noise. Whether the noise can be suppressed to the level of an ideal estimator without compromising the execution speed is an open question.

7. Variance calculation in the simulation

To estimate the variance of different covariance formulas in Fig. 2 and the variance of two different estimators for the fourth cumulant in Fig. 4, we carry out simple Monte Carlo simulations as follows.

First, we set a mean count rate for the channel that we are interested in. For example, we can set the count rate for four-body dissociation that generates particles (A, B, C, D) to be on average 2 dissociations per laser shot. Then we sample a Poisson distribution S times with the distribution's mean value being the count rate, which simulates an experiment with S laser shots. We obtain the covariance (cumulant) of these n particles' counts by computing their estimators \hat{e}^{conv} or \hat{e}^{new} . This gives us the covariance yield C_1 of the first simulated data set.

We repeat the process of data-set generation and estimator computing until we collect K such covariance yields $\{C_1, C_2, \dots, C_K\}$. Now we can compute the average value of these covariance yields μ and their standard deviation σ :

$$\begin{aligned} \mu &= \frac{\sum_{i=1}^K C_i}{K}, \\ \sigma &= \sqrt{\frac{\sum_{i=1}^K (C_i - \mu)^2}{K}}. \end{aligned} \quad (\text{A11})$$

The obtained variance σ^2 is an estimator of the actual variance $\text{var}(\hat{e})$. The higher the number of simulated data sets, the more accurate is the variance estimate; we use $K = 2000$ to produce Figs. 2 and 4.

The advantage of this simulation is that we can easily vary the count rate and data size S . Also, by adding additional channels (e.g., single ionization that only produces particle A), we can study the effect of uncorrelated background. The signal-to-noise ratio obtained from the simulations gives us an estimate of the time necessary to perform real experiments with sufficient statistics.

8. Variance calculation in the experiment

The variance calculation for the experiment is different from the simulation. As the experiment takes ~ 20 min, performing the same experiment 2000 times while keeping the laser intensity and sample pressure stable is too challenging. And repeating the experiment so many times in order to obtain the variance is not a practical proposition. Instead, there are methods to estimate the variance from the same data set by resampling techniques such as bootstrapping. Here, we use an idea of contingent covariance or “sliced” covariance to estimate the variance.

We divide the full data set into K' subsets with equal acquisition time (i.e., $S' = S/K'$ laser shots per subset) and perform the cumulant analysis on each subset. We calculate the four-fold cumulant for the momentum sum observable $\widehat{\chi}_4(\tilde{p}; l)$ using the corresponding estimators, where $l \in \{1, 2, \dots, K'\}$ and $K' = 50$.

Then we compute the mean value $\mu(\tilde{p})$ and the standard deviation $\sigma(\tilde{p})$ of the cumulant mapping using the following equations:

$$\mu(\tilde{p}) = \frac{\sum_{l=1}^{K'} \widehat{\chi}_4(\tilde{p}; l)}{K'},$$

$$\sigma(\tilde{p}) = \sqrt{\frac{\sum_{l=1}^{K'} [\widehat{\chi}_4(\tilde{p}; l) - \mu(\tilde{p})]^2}{K'}}. \quad (\text{A12})$$

Note that the variance σ^2 obtained in this manner is an estimator of the variance of the experiment with $S' = S/K'$ laser shots. Knowing that this variance varies as S^{-1} , we can estimate the uncertainty of the experiment with S laser shots:

$$\sigma_S(\tilde{p}) = \frac{\sigma(\tilde{p})}{\sqrt{K'}}. \quad (\text{A13})$$

We have tested this method with different values of K' . For $K' > 10$, the uncertainty $\sigma_S(\tilde{p})$ is practically constant, regardless of the actual K' value.

9. Variance calculation of compound estimators

Here we discuss the variance of compound estimators that contain two or more sums over the laser shots in the formula.

$$\begin{aligned} \text{var}(\hat{e}^{\text{conv}}) &= \text{var}\left(\frac{\sum_{i=1}^S N_i^A N_i^B \sum_{j=1}^S N_j^C N_j^D}{S^2}\right) \\ &= \left\langle \left(\frac{\sum_{i=1}^S N_i^A N_i^B \sum_{j=1}^S N_j^C N_j^D}{S^2}\right)^2 \right\rangle - \left\langle \frac{\sum_{i=1}^S N_i^A N_i^B \sum_{j=1}^S N_j^C N_j^D}{S^2} \right\rangle^2 \\ &= \frac{1}{S^4} \left\langle \sum_{i=1}^S N_i^A N_i^B \sum_{j=1}^S N_j^C N_j^D \sum_{i'=1}^S N_{i'}^A N_{i'}^B \sum_{j'=1}^S N_{j'}^C N_{j'}^D \right\rangle - \langle N^A N^B \rangle^2 \langle N^C N^D \rangle^2 \\ &= \text{different combinations of } (i, j, i', j') - \langle N^A N^B \rangle^2 \langle N^C N^D \rangle^2 \\ &= \frac{1}{S^4} \begin{cases} S \langle (N^A N^B N^C N^D)^2 \rangle & (i, j, i', j') = (i, i, i, i) \\ + 2S(S-1) \langle (N^A N^B)^2 N^C N^D \rangle \langle N^C N^D \rangle & \text{for } (i, j, i', j') = (i, i, i, j) \text{ or } (i, j, i, i) \\ + 2S(S-1) \langle N^A N^B (N^C N^D)^2 \rangle \langle N^A N^B \rangle & \text{for } (i, j, i', j') = (i, j, j, j) \text{ or } (j, j, i, j) \\ + 2S(S-1) \langle N^A N^B N^C N^D \rangle^2 & \text{for } (i, j, i', j') = (i, i, j, j) \text{ or } (i, j, j, i) \\ + S(S-1) \langle (N^A N^B)^2 \rangle \langle (N^C N^D)^2 \rangle & \text{for } (i, j, i', j') = (i, j, i, j) \\ + 4S(S-1)(S-2) \langle N^A N^B \rangle \langle N^C N^D \rangle \langle N^A N^B N^C N^D \rangle & \text{for } (i, j, i', j') = (i, i, i', j') \text{ or } (i, j, i', i) \\ + S(S-1)(S-2) \langle (N^A N^B)^2 \rangle \langle N^C N^D \rangle^2 & \text{or } (i, j, j, j') \text{ or } (i, j, i', i') \\ + S(S-1)(S-2) \langle N^A N^B \rangle^2 \langle (N^C N^D)^2 \rangle & \text{for } (i, j, i', j') = (i, j, i, j') \\ + [S(S-1)(S-2)(S-3) - S^4] \langle N^A N^B \rangle^2 \langle N^C N^D \rangle^2 & \text{for } (i, j, i', j') = (i, j, i', j') \end{cases} \\ &= O\left(\frac{1}{S}\right), \end{aligned} \quad (\text{A15})$$

$$\begin{aligned}
\text{var}(\hat{e}^{\text{new}}) &= \text{var}\left(\frac{\sum_{i=1}^S N_i^A N_i^B N_{i+\alpha}^C N_{i+\alpha}^D}{S}\right) \\
&= \left\langle \left(\frac{\sum_{i=1}^S N_i^A N_i^B N_{i+\alpha}^C N_{i+\alpha}^D}{S} \right)^2 \right\rangle - \left\langle \frac{\sum_{i=1}^S N_i^A N_i^B N_{i+\alpha}^C N_{i+\alpha}^D}{S} \right\rangle^2 \\
&= \frac{1}{S^2} \left\langle \sum_{i=1}^S N_i^A N_i^B N_{i+\alpha}^C N_{i+\alpha}^D \sum_{i'=1}^S N_{i'}^A N_{i'}^B N_{i'+\alpha}^C N_{i'+\alpha}^D \right\rangle - \langle N^A N^B \rangle^2 \langle N^C N^D \rangle^2 \\
&= \text{different combinations of } (i, i') - \langle N^A N^B \rangle^2 \langle N^C N^D \rangle^2 \\
&= \frac{1}{S^2} \begin{cases} S \langle (N^A N^B)^2 \rangle \langle (N^C N^D)^2 \rangle & \text{for } (i = i') \\ + 2S \langle N^A N^B \rangle \langle N^C N^D \rangle \langle N^A N^B N^C N^D \rangle & \text{for } (i + \alpha = i' \text{ or } i = i' + \alpha) \\ + [S(S-3) - S^2] \langle N^A N^B \rangle^2 \langle N^C N^D \rangle^2 & \text{otherwise} \end{cases} \\
&= O\left(\frac{1}{S}\right). \tag{A16}
\end{aligned}$$

According to the central limit theorem (CLT), as the number of measurements S increases, the distribution of the mean value becomes increasingly Gaussian type and the standard deviation of the mean value scales as $1/\sqrt{S}$, indicating convergence to a unique value as the number of measurements grows. This behavior is intuitive since averaging a larger number of independent measurements leads to a more precise estimation of the true mean.

It is interesting to note that the asymptotic behavior of the conventional estimator seems to be at odds with what is expected from the CLT. As seen from Eq. (A15), despite performing S^2 computations for this estimator, the variance contains a term proportional to S^{-1} , which becomes dominant for large data sets as $S \rightarrow \infty$. This apparent discrepancy is due to the dependencies between individual terms in \hat{e}^{conv} .

In the case of $\hat{e}^{\text{conv}} = \frac{1}{S^2} \sum_{i,j=1}^S N_i^A N_i^B N_j^C N_j^D$, many terms are not independent of each other. Consider, for example, the terms where $j = i + 1$ or $j = i + 2$. These terms share the same set of fragments A and B, giving a nonzero covariance:

$$\begin{aligned}
&\text{cov}(N_i^A N_i^B N_{i+1}^C N_{i+1}^D, N_i^A N_i^B N_{i+2}^C N_{i+2}^D) \\
&= \text{cov}(N_i^A N_i^B, N_i^A N_i^B) \langle N_{i+1}^C N_{i+1}^D \rangle \langle N_{i+2}^C N_{i+2}^D \rangle \\
&= \text{var}(N^A N^B) \langle N^C N^D \rangle^2 > 0, \tag{A17}
\end{aligned}$$

follows the same $\frac{1}{S}$ trend:

$$\begin{aligned}
\text{var}(\epsilon) &= \langle \epsilon^2 \rangle - \langle \epsilon \rangle^2 \\
&= \left\langle \left(\frac{1}{S} \sum_{i=1}^S X_i \right)^2 \right\rangle \left\langle \left(\frac{1}{S} \sum_{j=1}^S Y_j \right)^2 \right\rangle \left\langle \left(\frac{1}{S} \sum_{k=1}^S Z_k \right)^2 \right\rangle - \langle X \rangle^2 \langle Y \rangle^2 \langle Z \rangle^2 \\
&= \left(\frac{\text{var}(X)}{S} + \langle X \rangle^2 \right) \left\langle \left(\frac{1}{S} \sum_{j=1}^S Y_j \right)^2 \right\rangle \left\langle \left(\frac{1}{S} \sum_{k=1}^S Z_k \right)^2 \right\rangle - \langle X \rangle^2 \langle Y \rangle^2 \langle Z \rangle^2
\end{aligned}$$

where the approximation uses the delta method [see Eqs. (31) and (34) in [54]].

The presence of such dependencies leads to a variance term that scales differently than expected, ultimately limiting the convergence speed of the signal-to-noise ratio, which should naively scale as $S^{1/2}$. This departure from the usual behavior highlights the need for alternative estimators that can overcome the limitations of the conventional approach. The new estimator \hat{e}^{new} addresses these challenges by introducing an offset parameter that ensures the looping indices of two sets of fragments differ.

As is evident from Eq. (A16), the new estimator has a term that is proportional to S^{-1} , which is the dominant term at large S . Given the computational time for this new estimator, $T(\hat{e}^{\text{new}}) \propto S$ [as opposed to $T(\hat{e}^{\text{conv}}) \propto S^n (n > 1)$] and the fact that the variance calculations for the two estimators converge at the same rate $\propto S^{-1}$, the new estimator is computationally much more efficient. This modification estimates the observable of interest more accurately in the given computational time.

If three variables X, Y, Z are completely independent from each other, then the variance of the product of their individual means,

$$\epsilon = \left(\frac{1}{S} \sum_{i=1}^S X_i \right) \left(\frac{1}{S} \sum_{j=1}^S Y_j \right) \left(\frac{1}{S} \sum_{k=1}^S Z_k \right),$$

$$\begin{aligned}
&= \left(\frac{\text{var}(X)}{S} + \langle X \rangle^2 \right) \left(\frac{\text{var}(Y)}{S} + \langle Y \rangle^2 \right) \left(\frac{\text{var}(Z)}{S} + \langle Z \rangle^2 \right) - \langle X \rangle^2 \langle Y \rangle^2 \langle Z \rangle^2 \\
&= O\left(\frac{1}{S}\right).
\end{aligned} \tag{A18}$$

This property applies to an arbitrary number of random variables.

[1] J. H. D. Eland, Dynamics of fragmentation reactions from peak shapes in multiparticle coincidence experiments, *Laser Chem.* **11**, 259 (1991).

[2] M. Lavollée and H. Bergeron, Data treatment in multiparticle coincidence experiments: Two-step dissociation processes, *J. Phys. B: At., Mol. Opt. Phys.* **25**, 3101 (1992).

[3] A. Landers, T. Weber, I. Ali, A. Cassimi, M. Hattass, O. Jagutzki, A. Nauert, T. Osipov, A. Staudte, M. H. Prior, H. Schmidt-Böcking, C. L. Cocke, and R. Dörner, Photoelectron diffraction mapping: Molecules illuminated from within, *Phys. Rev. Lett.* **87**, 013002 (2001).

[4] L. Holmegaard, J. L. Hansen, L. Kalhøj, S. Louise Kragh, H. Stapelfeldt, F. Filsinger, J. Küpper, G. Meijer, D. Dimitrovski, M. Abu-Samha *et al.*, Photoelectron angular distributions from strong-field ionization of oriented molecules, *Nat. Phys.* **6**, 428 (2010).

[5] T. Jahnke, T. Weber, T. Osipov, A. Landers, O. Jagutzki, L. P. H. Schmidt, C. Cocke, M. Prior, H. Schmidt-Böcking, and R. Dörner, Multicoincidence studies of photo and Auger electrons from fixed-in-space molecules using the COLTRIMS technique, *J. Electron Spectrosc. Relat. Phenom.* **141**, 229 (2004).

[6] A. Staudte, S. Patchkovskii, D. Pavičić, H. Akagi, O. Smirnova, D. Zeidler, M. Meckel, D. M. Villeneuve, R. Dörner, M. Y. Ivanov, and P. B. Corkum, Angular tunneling ionization probability of fixed-in-space H₂ molecules in intense laser pulses, *Phys. Rev. Lett.* **102**, 033004 (2009).

[7] F. Allum, C. Cheng, A. J. Howard, P. H. Bucksbaum, M. Brouard, T. Weinacht, and R. Forbes, Multi-particle three-dimensional covariance imaging: “coincidence” insights into the many-body fragmentation of strong-field ionized D₂O, *J. Phys. Chem. Lett.* **12**, 8302 (2021).

[8] F. Légaré, K. F. Lee, I. V. Litvinyuk, P. W. Dooley, S. S. Wesolowski, P. R. Bunker, P. Dombi, F. Krausz, A. Bandrauk, D. M. Villeneuve, and P. B. Corkum, Laser Coulomb-explosion imaging of small molecules, *Phys. Rev. A* **71**, 013415 (2005).

[9] M. Pitzer, M. Kunitski, A. S. Johnson, T. Jahnke, H. Sann, F. Sturm, L. P. H. Schmidt, H. Schmidt-Böcking, R. Dörner, J. Stohner *et al.*, Direct determination of absolute molecular stereochemistry in gas phase by Coulomb explosion imaging, *Science* **341**, 1096 (2013).

[10] K. Fehre, S. Eckart, M. Kunitski, M. Pitzer, S. Zeller, C. Janke, D. Trabert, J. Rist, M. Weller, A. Hartung *et al.*, Enantioselective fragmentation of an achiral molecule in a strong laser field, *Sci. Adv.* **5**, eaau7923 (2019).

[11] A. J. Howard, M. Britton, Z. L. Streeter, C. Cheng, R. Forbes, J. L. Reynolds, F. Allum, G. A. McCracken, I. Gabalski, R. R. Lucchese *et al.*, Filming enhanced ionization in an ultrafast triatomic slingshot, *Commun. Chem.* **6**, 81 (2023).

[12] A. J. Howard, C. Cheng, R. Forbes, G. A. McCracken, W. H. Mills, V. Makhija, M. Spanner, T. Weinacht, and P. H. Bucksbaum, Strong-field ionization of water: Nuclear dynamics revealed by varying the pulse duration, *Phys. Rev. A* **103**, 043120 (2021).

[13] H. V. S. Lam, S. Yarlagadda, A. Venkatachalam, T. N. Wangjam, R. K. Kushawaha, C. Cheng, P. Svhra, A. Nomerotski, T. Weinacht, D. Rolles, and V. Kumarappan, Angle-dependent strong-field ionization and fragmentation of carbon dioxide measured using rotational wave packets, *Phys. Rev. A* **102**, 043119 (2020).

[14] Y. H. Jiang, A. Rudenko, O. Herrwerth, L. Foucar, M. Kurka, K. U. Kühnel, M. Lezius, M. F. Kling, J. van Tilborg, A. Belkacem, K. Ueda, S. Düsterer, R. Treusch, C. D. Schröter, R. Moshammer, and J. Ullrich, Ultrafast extreme ultraviolet induced isomerization of acetylene cations, *Phys. Rev. Lett.* **105**, 263002 (2010).

[15] S. Bhattacharyya, K. Borne, F. Ziae, S. Pathak, E. Wang, A. S. Venkatachalam, X. Li, N. Marshall, K. D. Carnes, C. W. Fehrenbach *et al.*, Strong-field-induced Coulomb explosion imaging of tribromomethane, *J. Phys. Chem. Lett.* **13**, 5845 (2022).

[16] M. Burt, K. Amini, J. W. Lee, L. Christiansen, R. R. Johansen, Y. Kobayashi, J. D. Pickering, C. Vallance, M. Brouard, and H. Stapelfeldt, Communication: Gas-phase structural isomer identification by Coulomb explosion of aligned molecules, *J. Chem. Phys.* **148**, 091102 (2018).

[17] J. L. Hansen, J. H. Nielsen, C. B. Madsen, A. T. Lindhardt, M. P. Johansson, T. Skrydstrup, L. B. Madsen, and H. Stapelfeldt, Control and femtosecond time-resolved imaging of torsion in a chiral molecule, *J. Chem. Phys.* **136**, 204310 (2012).

[18] L. Christensen, J. H. Nielsen, C. B. Brandt, C. B. Madsen, L. B. Madsen, C. S. Slater, A. Lauer, M. Brouard, M. P. Johansson, B. Shepperson *et al.*, Dynamic stark control of torsional motion by a pair of laser pulses, *Phys. Rev. Lett.* **113**, 073005 (2014).

[19] I. A. Bocharova, A. S. Alnaser, U. Thumm, T. Niederhausen, D. Ray, C. L. Cocke, and I. V. Litvinyuk, Time-resolved Coulomb-explosion imaging of nuclear wave-packet dynamics induced in diatomic molecules by intense few-cycle laser pulses, *Phys. Rev. A* **83**, 013417 (2011).

[20] S. De, M. Magrakvelidze, I. A. Bocharova, D. Ray, W. Cao, I. Znakovskaya, H. Li, Z. Wang, G. Laurent, U. Thumm, M. F. Kling, I. V. Litvinyuk, I. Ben-Itzhak, and C. L. Cocke, Following dynamic nuclear wave packets in N₂, O₂, and CO with few-cycle infrared pulses, *Phys. Rev. A* **84**, 043410 (2011).

[21] F. Allum, M. Burt, K. Amini, R. Boll, H. Köckert, P. K. Olshin, S. Bari, C. Bomme, F. Brause, B. Cunha de Miranda *et al.*, Coulomb explosion imaging of CH₃I and CH₂Cl photodissociation dynamics, *J. Chem. Phys.* **149**, 204313 (2018).

[22] M. Burt, R. Boll, J. W. L. Lee, K. Amini, H. Kockert, C. Vallance, A. S. Gentleman, S. R. Mackenzie, S. Bari, C. Bomme, S. Dusterer, B. Erk, B. Manschwetus, E. Muller, D. Rompotis, E. Savelyev, N. Schirmel, S. Techert, R. Treusch, J. Kupper *et al.*, Coulomb-explosion imaging of concurrent CH_2BrI photodissociation dynamics, *Phys. Rev. A* **96**, 043415 (2017).

[23] X. Ding, R. Forbes, M. Kübel, K. F. Lee, M. Spanner, A. Y. Naumov, D. Villeneuve, A. Stolow, P. Corkum, and A. Staudte, Threshold photodissociation dynamics of NO_2 studied by time-resolved cold target recoil ion momentum spectroscopy, *J. Chem. Phys.* **151**, 174301 (2019).

[24] F. Allum, N. Anders, M. Brouard, P. Bucksbaum, M. Burt, B. Downes-Ward, S. Grundmann, J. Harries, Y. Ishimura, H. Iwayama *et al.*, Multi-channel photodissociation and XUV-induced charge transfer dynamics in strong-field-ionized methyl iodide studied with time-resolved recoil-frame covariance imaging, *Faraday Discuss.* **228**, 571 (2021).

[25] D. M. Bittner, K. Gope, and D. Strasser, Time-resolved dissociative ionization and double photoionization of CO_2 , *J. Chem. Phys.* **153**, 194201 (2020).

[26] C. Cheng, V. Singh, S. Matsika, and T. Weinacht, Strong field double ionization of formaldehyde investigated using momentum resolved covariance imaging and trajectory surface hopping, *J. Phys. Chem. A* **126**, 7399 (2022).

[27] K. Gope, I. Luzon, and D. Strasser, N-NO & NN-O bond cleavage dynamics in two-and three-body Coulomb explosion of the N_2O^{2+} dication, *Phys. Chem. Chem. Phys.* **21**, 13730 (2019).

[28] T. Endo, S. P. Neville, V. Wanie, S. Beaulieu, C. Qu, J. Deschamps, P. Lassonde, B. E. Schmidt, H. Fujise, M. Fushitani *et al.*, Capturing roaming molecular fragments in real time, *Science* **370**, 1072 (2020).

[29] E. Wang, X. Shan, L. Chen, T. Pfeifer, X. Chen, X. Ren, and A. Dorn, Ultrafast proton transfer dynamics on the repulsive potential of the ethanol dication: roaming-mediated isomerization versus Coulomb explosion, *J. Phys. Chem. A* **124**, 2785 (2020).

[30] N. Ekanayake, T. Severt, M. Nairat, N. P. Weingartz, B. M. Farris, B. Kaderiya, P. Feizollah, B. Jochim, F. Ziaeef, K. Borne *et al.*, H_2 roaming chemistry and the formation of H_3^+ from organic molecules in strong laser fields, *Nat. Commun.* **9**, 5186 (2018).

[31] E. Livshits, I. Luzon, K. Gope, R. Baer, and D. Strasser, Time-resolving the ultrafast H_2 roaming chemistry and H_3^+ formation using extreme-ultraviolet pulses, *Commun. Chem.* **3**, 49 (2020).

[32] K. Gope, E. Livshits, D. M. Bittner, R. Baer, and D. Strasser, Two pathways and an isotope effect in H_3^+ formation following double ionization of methanol, *Nat. Sci.* **1**, e10022 (2021).

[33] I. Luzon, E. Livshits, K. Gope, R. Baer, and D. Strasser, Making sense of Coulomb explosion imaging, *J. Phys. Chem. Lett.* **10**, 1361 (2019).

[34] C. Cheng, R. Forbes, A. J. Howard, M. Spanner, P. H. Bucksbaum, and T. Weinacht, Momentum-resolved above-threshold ionization of deuterated water, *Phys. Rev. A* **102**, 052813 (2020).

[35] C. Cheng, P. Vindel-Zandbergen, S. Matsika, and T. Weinacht, Electron correlation in channel-resolved strong-field molecular double ionization, *Phys. Rev. A* **100**, 053405 (2019).

[36] R. Boll, J. M. Schäfer, B. Richard, K. Fehre, G. Kastirke, Z. Jurek, M. S. Schöffler, M. M. Abdullah, N. Anders, T. M. Baumann *et al.*, X-ray multiphoton-induced Coulomb explosion images complex single molecules, *Nat. Phys.* **18**, 423 (2022).

[37] X. Li, A. Rudenko, M. S. Schöffler, N. Anders, T. M. Baumann, S. Eckart, B. Erk, A. De Fanis, K. Fehre, R. Dorner, L. Foucar, S. Grundmann, P. Grychtol, A. Hartung, M. Hofmann, M. Ilchen, C. Janke, G. Kastirke, M. Kircher, K. Kubicek *et al.*, Coulomb explosion imaging of small polyatomic molecules with ultrashort X-ray pulses, *Phys. Rev. Res.* **4**, 013029 (2022).

[38] C. S. Slater, S. Blake, M. Brouard, A. Lauer, C. Vallance, C. S. Bohun, L. Christensen, J. H. Nielsen, M. P. Johansson, and H. Stapelfeldt, Coulomb-explosion imaging using a pixel-imaging mass-spectrometry camera, *Phys. Rev. A* **91**, 053424 (2015).

[39] Y. Park, I. Noda, and Y. M. Jung, Novel developments and applications of two-dimensional correlation spectroscopy, *J. Mol. Struct.* **1124**, 11 (2016).

[40] L. J. Frasinski, Covariance mapping techniques, *J. Phys. B: At. Mol. Opt. Phys.* **49**, 152004 (2016).

[41] L. Frasinski, K. Codling, and P. Hatherly, Covariance mapping: A correlation method applied to multiphoton multiple ionization, *Science* **246**, 1029 (1989).

[42] C. Vallance, D. Heathcote, and J. W. Lee, Covariance-map imaging: A powerful tool for chemical dynamics studies, *J. Phys. Chem. A* **125**, 1117 (2021).

[43] T. Driver, B. Cooper, R. Ayers, R. Pipkorn, S. Patchkovskii, V. Averbukh, D. R. Klug, J. P. Marangos, L. J. Frasinski, and M. Edelson-Averbukh, Two-dimensional partial-covariance mass spectrometry of large molecules based on fragment correlations, *Phys. Rev. X* **10**, 041004 (2020).

[44] C. S. Slater, S. Blake, M. Brouard, A. Lauer, C. Vallance, J. J. John, R. Turchetta, A. Nomerotski, L. Christensen, J. H. Nielsen, M. P. Johansson, and H. Stapelfeldt, Covariance imaging experiments using a pixel-imaging mass-spectrometry camera, *Phys. Rev. A* **89**, 011401 (2014).

[45] J. W. McManus, T. Walmsley, K. Nagaya, J. R. Harries, Y. Kumagai, H. Iwayama, M. N. R. Ashfold, M. Britton, P. H. Bucksbaum, B. Downes-Ward *et al.*, Disentangling sequential and concerted fragmentations of molecular polycations with covariant native frame analysis, *Phys. Chem. Chem. Phys.* **24**, 22699 (2022).

[46] J. D. Pickering, B. Shepperson, B. A. K. Hübschmann, F. Thorning, and H. Stapelfeldt, Alignment and imaging of the CS_2 dimer inside helium nanodroplets, *Phys. Rev. Lett.* **120**, 113202 (2018).

[47] J. D. Pickering, B. Shepperson, L. Christiansen, and H. Stapelfeldt, Femtosecond laser induced coulomb explosion imaging of aligned ocs oligomers inside helium nanodroplets, *J. Chem. Phys.* **149**, 154306 (2018).

[48] C. Schouder, A. S. Chatterley, F. Calvo, L. Christiansen, and H. Stapelfeldt, Structure determination of the tetracene dimer in helium nanodroplets using femtosecond strong-field ionization, *Struct. Dyn.* **6**, 044301 (2019).

[49] C. Schouder, A. S. Chatterley, M. Johny, F. Hübschmann, A. F. Al-Refaie, F. Calvo, J. Küpper, and H. Stapelfeldt, Laser-induced coulomb explosion imaging of $(\text{C}_6\text{H}_5\text{Br})_2$ and $\text{C}_6\text{H}_5\text{Br}-\text{I}_2$ dimers in helium nanodroplets using a tpx3cam, *J. Phys. B: At., Mol. Opt. Phys.* **54**, 184001 (2021).

[50] J. D. Pickering, K. Amini, M. Brouard, M. Burt, I. J. Bush, L. Christensen, A. Lauer, J. H. Nielsen, C. S. Slater, and H.

Stapelfeldt, Communication: Three-fold covariance imaging of laser-induced Coulomb explosions, *J. Chem. Phys.* **144**, 161105 (2016).

[51] D. You, H. Fukuzawa, Y. Luo, S. Saito, M. Berholts, T. Gaumnitz, M. Huttula, P. Johnsson, N. Kishimoto, H. Myllynen *et al.*, Multi-particle momentum correlations extracted using covariance methods on multiple-ionization of diiodomethane molecules by soft-X-ray free-electron laser pulses, *Phys. Chem. Chem. Phys.* **22**, 2648 (2020).

[52] C. Cheng, L. J. Frasinski, G. Moğol, F. Allum, A. J. Howard, D. Rolles, P. H. Bucksbaum, M. Brouard, R. Forbes, and T. Weinacht, Multiparticle cumulant mapping for coulomb explosion imaging, *Phys. Rev. Lett.* **130**, 093001 (2023).

[53] V. Zhaunerchyk, L. J. Frasinski, J. H. D. Eland, and R. Feifel, Theory and simulations of covariance mapping in multiple dimensions for data analysis in high-event-rate experiments, *Phys. Rev. A* **89**, 053418 (2014).

[54] L. J. Frasinski, Cumulant mapping as the basis of multi-dimensional spectrometry, *Phys. Chem. Chem. Phys.* **24**, 20776 (2022).

[55] J. Mikosch and S. Patchkovskii, Coincidence and covariance data acquisition in photoelectron and-ion spectroscopy. I. Formal theory, *J. Mod. Opt.* **60**, 1426 (2013).

[56] J. Mikosch and S. Patchkovskii, Coincidence and covariance data acquisition in photoelectron and-ion spectroscopy. II. Analysis and applications, *J. Mod. Opt.* **60**, 1439 (2013).

[57] C. Cornaggia, Statistical analysis of fragmentation channels of small multicharged molecular ions, *J. Phys. B: At., Mol. Opt. Phys.* **45**, 085602 (2012).

[58] A. T. Eppink and D. H. Parker, Velocity map imaging of ions and electrons using electrostatic lenses: Application in photo-electron and photofragment ion imaging of molecular oxygen, *Rev. Sci. Instrum.* **68**, 3477 (1997).

[59] A. Zhao, M. van Beuzekom, B. Bouwens, D. Byelov, I. Chakaberia, C. Cheng, E. Maddox, A. Nomerotski, P. Svihra, J. Visser *et al.*, Coincidence velocity map imaging using Tpx3Cam, a time stamping optical camera with 1.5 ns timing resolution, *Rev. Sci. Instrum.* **88**, 113104 (2017).

[60] D. Aglagul, B. Kaufman, C. Cheng, T. Weinacht, T. Saule, C. A. Trallero-Herrero, and A. Nomerotski, A simple approach for characterizing the spatially varying sensitivity of microchannel plate detectors, *Rev. Sci. Instrum.* **93**, 075108 (2022).

[61] C. Cheng, Z. L. Streeter, A. J. Howard, M. Spanner, R. R. Lucchese, C. W. McCurdy, T. Weinacht, P. H. Bucksbaum, and R. Forbes, Strong-field ionization of water. II. electronic and nuclear dynamics en route to double ionization, *Phys. Rev. A* **104**, 023108 (2021).

[62] L. J. Frasinski, V. Zhaunerchyk, M. Mucke, R. J. Squibb, M. Siano, J. H. D. Eland, P. Linusson, P. v. d. Meulen, P. Salen, R. D. Thomas, M. Larsson, L. Foucar, J. Ullrich, K. Motomura, S. Mondal, K. Ueda, T. Osipov, L. Fang, B. F. Murphy *et al.*, Dynamics of hollow atom formation in intense X-ray pulses probed by partial covariance mapping, *Phys. Rev. Lett.* **111**, 073002 (2013).